Ultrasound in Medicine & Biology 52 (2026) 891–907

Contents lists available at ScienceDirect

Ultrasound in Medicine & Biology

journal homepage: www.elsevier.com/locate/ultrasmedbio

Review

Clinical Translation of Ultrasound Localization Microscopy: A Narrative Review of Current Applications and Future Directions

Sylvain Bodard [a,b,c,*], Louise Denis [c], Basile Pradier [b,c], Georges Chabouh [d], Olivier Hélénon [b], Jean-Michel Correas [b,c], Leonardo V. Riella [a], Olivier Couture [c]

[a] Harvard Medical School, Center for Transplantation Sciences, Massachusetts General Hospital, Boston, MA, USA
[b] Université Paris Cité, AP-HP, Hôpital Universitaire Necker Enfants Malades, Service d'Imagerie Adulte, Paris, France
[c] Sorbonne Université, Laboratoire d'Imagerie Biomédicale (LIB), Paris, France
[d] Columbia University, Ultrasound Elasticity Imaging Laboratory, New York, NY, USA

ARTICLE INFO

Keywords:
Diagnostic imaging
Ultrasonography
Biomarkers
Microvessels
Blood flow velocity

ABSTRACT

Microvascular dysfunction plays a pivotal role in numerous diseases, often preceding clinical symptoms and structural changes. Ultrasound localization microscopy (ULM) is an emerging ultrasound imaging modality that enables *in vivo* visualization of microvascular structures with unprecedented resolution. This narrative review aimed to examine the recent clinical applications of ULM and its role in biomarker development. It was conducted following PRISMA 2020 guidelines and included 33 articles published up to November 2025, focusing on ULM in human studies. Inclusion criteria targeted studies evaluating ULM's clinical applications and biomarkers. Data extraction encompassed imaging protocols, biomarkers and outcomes, with study quality assessed using the Newcastle–Ottawa Scale. ULM demonstrates significant promise across various organs. In kidney applications, ULM and its novel variant, sensing ULM, identified glomeruli and microvascular density as biomarkers for kidney disease and allograft dysfunction. In the brain, transcranial ULM enabled microvascular mapping with a resolution of 25 μm, aiding the evaluation of Moyamoya disease. ULM has also shown potential in detecting inflammatory changes in the carotid artery, myocardial microcirculation and testicular vascular architecture. Oncology applications include monitoring tumor vascularity and therapy response, revealing early microvascular changes undetectable by conventional imaging. Future technical improvements, such as higher-frame-rate clinical scanners, real-time data processing and clinical 3D imaging capabilities, are necessary to overcome current limitations. To conclude, ULM is on the verge of clinical translation, offering significant potential for developing microvascular biomarkers across various tissues and diseases. The medical community must now adopt and refine ULM applications and establish their role in routine clinical practice.

Introduction

The assessment of human microvasculature has gained significant attention due to its critical role in delivering oxygen and nutrients to tissues and maintaining homeostasis [1]. Microvascular dysfunction is implicated in various diseases, including arteriosclerosis, diabetes, cancer and kidney disorders, often preceding clinical symptoms and morphological changes [2–6]. Early detection is crucial to prevent long-term complications [2].

The current gold standard for evaluating tissue microvasculature is biopsy with histopathological analysis; however, it is invasive, carries risks and provides limited sampling that may not capture tissue heterogeneity [7,8]. Imaging modalities such as magnetic resonance imaging (MRI) and computed tomography (CT) offer perfusion assessments but lack the resolution to visualize microvascular networks [9–12], while Doppler ultrasound (US) is limited to detecting larger vessels with rapid blood flow [13]. Contrast-enhanced US (CEUS) improves sensitivity but

Abbreviations: AKI, Acute Kidney Injury; AU, Arbitrary Units; CEUS, Contrast-Enhanced Ultrasound; CTA, Computed Tomography Angiography; FSH, Follicle-Stimulating Hormone; FNH, Focal Nodular Hyperplasia; HCC, Hepatocellular Carcinoma; LM, Liver Metastases; LN(s), Lymph Node(s); MB(s), Microbubble(s); MD, Moyamoya Disease; MRI, Magnetic Resonance Imaging; NOA, Non-Obstructive Azoospermia; OA, Obstructive Azoospermia; CT, Computed Tomography; RECIST, Response Evaluation Criteria in Solid Tumors; RT, Radiotherapy; SRI, Super-Resolution Imaging; SRUS, Super-Resolution Ultrasound; sULM, Sensing Ultrasound Localization Microscopy; SWE, Shear-Wave Elastography; TNBC, Triple-Negative Breast Cancer; ULM, Ultrasound Localization Microscopy; US, Ultrasound

* Corresponding author at: Harvard Medical School, Center for Transplantation Sciences, Massachusetts General Hospital, 55 Fruit Street, Boston, MA, 02114, USA.
E-mail address: sylvain.bodard@aphp.fr (S. Bodard).
Registration: NIHR-PROSPERO #CRD42025640156

https://doi.org/10.1016/j.ultrasmedbio.2025.12.011
Received 30 July 2025; Revised 15 November 2025; Accepted 18 December 2025

remains restricted by resolution limitations, making it challenging to capture microvascular heterogeneity [14–16].

Ultrasound localization microscopy (ULM) is an emerging technique that enables *in vivo* visualization of microvascular structures and blood flow at very high resolution. ULM leverages CEUS cine loops with injected microbubbles (MBs), which are localized with a subwavelength precision and then tracked frame-by-frame to reconstruct detailed vascular images and measure blood flow dynamics [17–21]. Compared to conventional CEUS and Doppler methods, ULM overcomes sound diffraction limitations and offers superior visualization of microvascular complexity. Open-source tools have further facilitated access to ULM technology, promoting standardization and collaborative research efforts [16,22–24].

Super-resolution US (SRUS) imaging is a general domain that includes any techniques that can surpass the classical diffraction limit. ULM is a particular technique that localizes individual injectable MBs to achieve super-resolution. ULM is used in many SRUS cases.

Despite its potential, clinical translation of ULM remains challenging due to the need for high-frame-rate US systems and stable imaging conditions, which are not yet widely available in clinical practice [13,20,25]. However, recent advancements suggest that ULM may soon be feasible for broader clinical applications. A promising approach involves repurposing routinely acquired CEUS loops for ULM analysis, offering a resource-efficient method to explore microvascular structures without additional imaging [26,27].

This review explores the current clinical applications of ULM, highlighting its potential within existing technological constraints and its role in advancing biomarker discovery and validation.

Materials and methods

A PubMed search of MEDLINE articles was conducted following the PRISMA 2020 guidelines [28] and registered with NIHR-PROSPERO (CRD42025640156). The search targeted human studies published up to November 2025 that evaluated ULM.

The search aimed to identify articles containing the following keywords in the title and/or abstract: (“ultrasound localization microscopy” OR “super-resolution ultrasound”). A total of 252 articles were retrieved. Filters were applied to ensure the availability of studies conducted in humans. Reviews, meta-analyses and animal studies were excluded, resulting in 33 articles discussed in this review (Table 1).

Two reviewers independently screened and extracted data using a standardized form. The details extracted included author and publication information, study design, population characteristics, imaging protocols and ULM-specific techniques, key study outcomes and reported biomarkers. In addition, references from previously published reviews on clinical ULM were incorporated to enrich the scope of the procedure and ensure comprehensive coverage of the field [13,26,29]. The methodological quality of the included studies was assessed using the Newcastle–Ottawa Scale [30]. The risk of bias in individual studies was evaluated with the Newcastle–Ottawa Scale to ensure the validity of the results.

The findings were summarized in a narrative synthesis, which provides an overview of ULM’s clinical applications, emerging biomarkers and technical advancements. The Supplementary Section details ULM principles.

Results

The microvasculature is essential in cerebral pathologies such as stroke, vascular dementia and neurodegenerative conditions [31–34]. Indeed, the cerebral microvasculature plays a pivotal role in maintaining neuronal health by ensuring adequate oxygen and nutrient delivery, regulating the blood–brain barrier and clearing metabolic waste. Early alterations in microvascular structure or flow often precede the onset of overt ischemic lesions or cognitive decline, making microvascular assessment a sensitive indicator of cerebrovascular and neurodegenerative disease progression [33,34]. However, current imaging techniques like CT angiography (CTA) and magnetic resonance angiography cannot image microvessels or provide detailed hemodynamic information. By providing subwavelength visualization of cortical and deep microvessels together with quantitative flow mapping, ULM could bridge the current diagnostic gap between macrovascular imaging and histopathology. Clinically, this could enable earlier detection of microcirculatory dysfunction in stroke, vascular dementia or Moyamoya disease (MD), refine prognosis and guide therapeutic monitoring where conventional MRI or CTA remain insensitive to microvascular remodeling [31–34].

Demené et al. [35] measured vascular and hemodynamic parameters transcranially with a programmable research scanner operated at 800 frames/s in 3 patients using unfocused diverging waves optimized for brain imaging, achieving resolutions as fine as 25 μm and a depth penetration up to 120 mm. Flow velocity maps were generated for vessels 1 mm in diameter or smaller, characterizing both healthy and dysfunctional vascular networks. These included functional information such as flow speed and direction within the microvasculature. Cross-sectional flow speed analysis was performed at different points in the cardiac cycle, with the central median speed measured at 24.9 cm/s and increasing to 33.1 cm/s during diastole. These parameters may be future biomarkers for assessing clotting risks or aneurysm rupture.

Imaging was conducted through the temporal sutures, focusing on the central cerebrovascular area. However, the authors proposed that utilizing the contralateral temporal window, combined with adjustments to frequency and elevation focus, could enable whole-brain imaging. Moreover, advancements in real-time processing could improve probe positioning and facilitate the diagnosis of smaller pathologies, such as microaneurysms or subtle vascular defects.

On the other hand, Knieling et al. used transfontanellar ULM to observe the human microvasculature in neonatal patients undergoing treatment for life-threatening malformations, forming direct connections between the cerebral arterial and venous systems. They observed that neuroendovascular treatment of neonatal arteriovenous malformations caused remodeling and reorganization of the cerebral vasculature by also activating corticomedullary vascular connections. ULM has thus enabled them to follow microstructural vascular changes in human neonates with high spatio-temporal resolution [36]. ULM may provide a novel clinical translatable tool, particularly including cerebral imaging in very young patients. Recently, Regensburger et al. demonstrated the first application of transfontanellar ULM to provide super-resolution and time-resolved information on the microvascular structure and circulation in perinatal stroke. According to the authors, this might accelerate the diagnosis of acute perinatal stroke in newborns with seizures and, thus, influence clinical decisions [37].

Recently, Huang et al. obtained a precise distribution of microvasculature in deep cerebral regions in a patient with intracranial pressure with a resolution of ~30 μm, using an everyday bedside US scanner combined with a computerized super-resolution reconstruction algorithm. Moreover, they found that capillaries and large vessels may have different responding behaviors when the intracranial pressure value is abated, and they proposed a theory to explain these contradictions in terms of a time effect and the nature of the dynamic ensemble [38].

Denis et al. evaluated the utility of 2D transcranial ULM using a widely available clinical US scanner operated at low frame rates (around 30 frame/s) in 9 patients with MD—a rare chronic arteriopathy characterized by a compensatory network of dense, tortuous perforating small arteries. Their study produced density maps and reconstructed perforating arteries with diameters as small as 80 μm. Although the number and population of vessels appeared greater in patients with MD compared to controls, these differences were not statistically significant [39]. Similarly, the reconstructions suggested potential morphological differences

Table 1
Studies included in the review

Organ/disease	Paper	Structure visualized	Human participants	Specificity	Methods used transmission/frame rate
Brain	Demené et al. [35]	Brain; deep vasculature	2 patients, one with aneurysm (distal. right MCA), one with MM-like disease	Adaptive speckle tracking to correct for motion artefacts and for ultrasonic-wave aberrations induced during transcranial propagation	2 MHz transmission, 800 Hz frame rate
	Knieling et al. [36]	Brain	7 neonatal patients with cerebral vascular malformations. Control group of 8 patients	Transfontanellar	14 Hz frame rate
	Huang et al. [38]	Brain	Patient with intracranial pressure		2 MHz frame rate
	Denis et al. [39]	Brain; MCA region	9 with MM disease, 15 controls with ischemic stoke not related to perforating arteries		2 MHz transmission, 19 Hz frame rate
	Regensburger et al. [37]	Brain	1 late-term newborn with an acute ischemic stroke in the middle cerebral artery	Transfontanellar	N.A.
Carotid artery	Goudot et al. [44]	Carotid wall vasa vasorum	5 active Takayasu arteritis, 11 quiescent Takayasu arteritis		6.4 MHz transmission, 500 Hz frame rate
	Goudot et al. [44]	Carotid wall vasa vasorum	5 active Takayasu arteritis	ClinicalTrials.gov Identifier: NCT03956394	
	Leroy et al. [45]	Atherosclerotic carotid plaques	26 patients included, 18 patients with analyzable CEUS images classified as group A (absence of neovascularisation, $n = 10$) and group B (presence of neovascularisation, $n = 8$)		7 MHz transmission, 500 Hz frame rate
Heart	Yan et al. [47]	Myocardial vasculature	2 patients with impaired myocardial. Function, 2 controls	Custom data acquisition and processing pipeline involving selection of diastolic phase, removal of MB signals from tissue signals by singular value decomposition, two-stage image registration and rigid image registration to align images across different cardiac cycles	2.4 and 1.7 MHz transmission, 305 Hz frame rate
Liver	Huang et al. [16]	Healthy liver	1 patient with healthy liver and 1 patient with acute-on-chronic liver failure		6 MHz transmission, 415.3 and 490 Hz frame rate
Kidney	Huang et al. [16]	Native kidney	1 healthy kidney		6 MHz transmission, 250.4 Hz frame rate
	Bodard et al. [61]	Allograft kidney	35 kidney allografts for optimization, 7 kidney allografts for assessment		3 MHz transmission, 14–64 Hz frame rate depending on depth
	Denis et al. [39]	Allograft kidney (glomeruli)	5 allograft kidneys	Double filtering and double tracking of MBs, identification of functional structures (glomeruli)	15 MHz transmission, 16–64 Hz frame rate depending on depth
	Bodard et al. [57]	Native kidney	15 native kidneys compared to 5 kidney allografts	Double filtering and double tracking of MBs, identification of functional structures (glomeruli)	3 MHz transmission, 0.5–5.5 Hz frame rate
	Huang et al. [63]	Allograft kidney	16 kidney allografts: 6 normal allograft functions and 10 allograft malfunctions		80 Hz frame rate
	Huang et al. [63]	Native kidney (AKI and controls)	62 with sepsis, 38 with AKI and 21 controls	MB signal separation method using Kalman-filter based tracking applied to high frame rate clinical. Scanner without MB dilution	5.2 MHz transmission, 500 Hz frame rate
	Chen et al. [60]	Native kidney (chronic kidney disease)	3 individuals with kidney disease, 4 healthy controls		3 MHz transmission, high-frame-rate data acquisition
	Huang et al. [63]	Healthy kidney	One healthy volunteer (25-y-old female)	To optimize *in vivo* data acquisition	
	Grieshaber-Bouyer Mandelbaum et al. [62]	Neonatal kidneys	5 human neonate		
Lower limb	Harput et al. [100]	Lower limb	3 healthy volunteers	Improved motion correction	Transmission 6 MHz, 13 Hz frame rate
Prostate	Solomon et al. [74]	Prostate	1 participant	Improvement to sparse recovery process to improve MB tracking, online estimation process	10 Hz frame rate
Testes	Li et al. [72]	Testes	76 infertile patients and 15 healthy controls	Graph-based tracking with the Kalman motion model algorithm	20 Hz frame rate
	Li et al. [73]	Testes	36 NOA patients, 58 OA patients	Multiple logistic regression analysis to integrate hormone and vascular criteria for diagnosis	114 Hz frame rate
Thyroid	Hansen-Shearer et al. [93]	Thyroid	1 participant	3-D transcutaneous using a row–column array with coherence-based beamforming and rolling sub-aperture processing	Effective frame rate: up to 4000

(*continued on next page*)

Table 1 (*Continued*)

Organ/disease	Paper	Structure visualized	Human participants	Specificity	Methods used transmission/frame rate
Tumors	Opacic et al. [88]	Various solid tumors	3 cancer patients	Addition of parameters that combine textural and functional differences; (i) distances to vessel with low velocities and (ii) distances to vessel with high velocities.	10 MHz transmission
	Dencks et al. [87]	Breast cancer	4 patients, 8 measurements (2 per examination)	Clinical pilot study	7–14 MHz transmission, 15 Hz frame rate
	Kanoulas et al. [75]	Prostate cancer	1 participant		7.8 MHz transducer, 500 Hz frame rate
	Huang et al. [16]	Breast cancer	1 tumor after neoadjuvant chemotherapies		6 MHz transmission, 622 Hz frame rate
	Huang et al. [16]	Pancreatic tumor	1 mixed cystic solid mass of 164 × 65 × 66 mm		6 MHz transmission, 415.3 Hz frame rate
	Zhu et al. [94]	Lymph nodes	10 patients with a variety of malignancies, 6 with lymph node metastasis and 4 with benign lymphadenopathy		5.6 MHz transmission, 20 Hz frame rate
	Morris et al. [76]	Breast cancer	Repeatability study; 12 breast cancer patients. Response assessment study; 11 breast cancer patients	Averaging over of multiple image planes	5 MHz transmission
	Porte et al. [98]	Breast cancer	11 breast cancer patients	Improvements to motion correction and comparison of contrast agent dose, injection speed and timing	5 MHz, 10 Hz frame rate
	Lei et al. [89]	Breast cancer	97 breast cancer patients	Combined with shear-wave elastography	80 Hz frame rate
	Zeng et al. [91]	Liver tumors	47 patients with focal liver lesions	30 hepatocellular carcinomas, 11 liver metastases, 6 focal nodular hyperplasias	3.1 MHz transmission, 350–500 Hz frame rate
	Bodard et al. [57]	Renal tumors	6 renal tumors compared to 6 renal pseudotumors	Distinction between tumors and pseudotumors based on the presence or absence of glomeruli	1.8–6.2 MHz transmission, 39–44 images/s
	Li et al. [90]	Breast cancer	83 patients with breast tumors. 55 patients with malignant lesion, 28 patients with benign lesion.	Prospective and multicenter study, publication of the protocol	N/A

AKI, acute kidney injury; Hz, hertz; MB, microbubbles; MCA, middle cerebral artery; MHz, megahertz; MM, Moya Moya; NOA, non-obstructive azoospermia; OA, obstructive azoospermia; s, second; SVD, singular value decomposition; μm, micrometer.

in the pathological vascular networks of MD, but these findings lacked statistical significance.

The authors also emphasized the potential for exploring additional biomarkers, such as flow velocity and pulsatility, which could be assessed using higher frame rate scanners (Fig. 1) [39,40].

A detailed summary of the key quantitative and qualitative findings extracted from each included study is provided in Table 2.

Carotid artery

Evaluating arterial wall inflammation in vasculitis, such as Takayasu's arteritis (TA), is crucial but remains clinically challenging. This includes monitoring the structure and flow dynamics of the vasa vasorum, a microvascular network within the arterial wall subject to heightened metabolic activity and microvessel enrichment [41,42]. Characterizing these affected regions is essential for distinguishing between active and quiescent phases of the disease and guiding appropriate immunosuppressive therapy. ULM offers the unique capability to non-invasively visualize and quantify the vasa vasorum, providing dynamic metrics of microvascular density and flow that reflect inflammatory activity within the arterial wall. Clinically, this could enable earlier detection of relapse, improve disease activity monitoring beyond conventional Doppler or positron emission tomography/CT, and guide timely adjustments of immunosuppressive therapy.

In a pilot study, Goudot et al. demonstrated the potential of ULM to detect and quantify inflammation-related changes in the vasa vasorum of the carotid wall in TA. They observed a higher number of MBs in active disease (121 MBs/s) compared to the quiescent phase (10 MBs/s, $p < 0.001$). Additionally, longer MB paths were recorded (43 mm in active disease vs. 4 mm in quiescent, $p < 0.001$), along with an increased perfusion score (3.9 mm^3/s in active disease vs. 0.5 mm^3/s in quiescent, $p < 0.001$). These metrics reflected a marked enhancement of the microvascular network during the active phase of TA (Fig. 2).

This quantification of MB passage strongly correlated with arterial wall inflammation, suggesting it could be a biomarker for disease activity. However, the study did not include a healthy control group, as the normal carotid arterial wall is too thin for ULM-based measurements [43]. They confirmed these results in a clinical trial (ClinicalTrials.gov Identifier: NCT03956394) of 5 patients in which they demonstrated that vasa vasorum interna were present in humans in the case of active TA and emphasized the involvement of the intima in the pathological process [44].

More recently, Leroy et al. [45] confirmed that ULM provides a precise picture of plaque neovascularisation in patients and could be used as a non-invasive imaging technique to assess carotid plaque vulnerability.

Heart

Coronary heart disease remains the leading cause of mortality worldwide [46], yet imaging the myocardial microvasculature poses unique challenges. These include cardiac tissue rigid and non-rigid motion, the need for a large field of view and the small aperture and high aberrations from the rib [47]. The myocardial microcirculation plays a critical role in oxygen delivery and metabolic regulation of the heart, and its impairment is often an early and potentially reversible event preceding macrovascular obstruction. Microvascular dysfunction has been implicated in conditions such as ischemia with non-obstructive coronary arteries, diabetic cardiomyopathy and heart failure with preserved ejection fraction, where conventional angiography fails to detect abnormalities [46,47]. ULM could provide direct, high-resolution visualization of myocardial microvascular networks and quantify flow heterogeneity across cardiac regions. This capability may help identify early microvascular dysfunction before irreversible myocardial damage occurs, guide

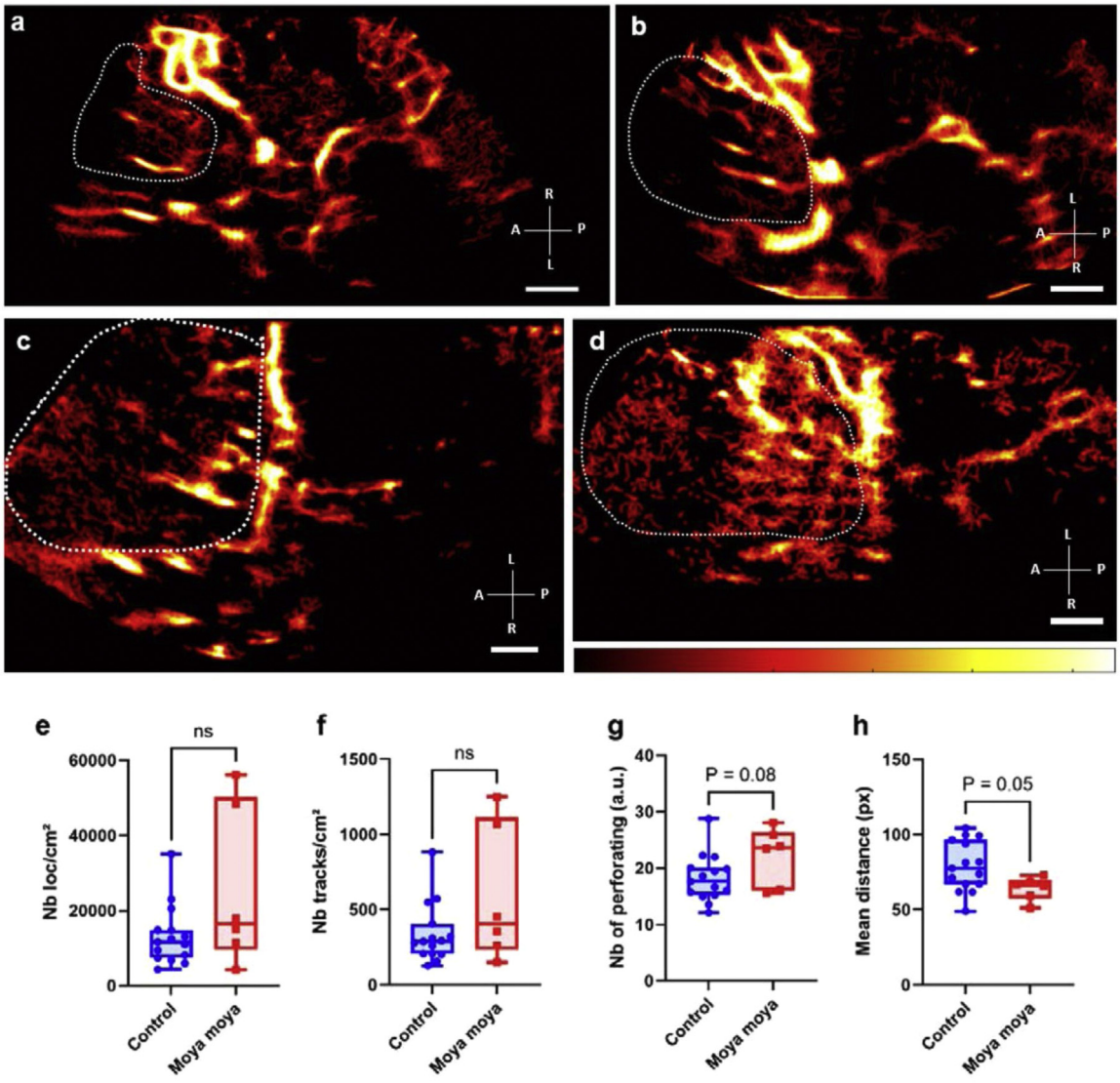

Figure 1. Comparison of ULM density maps between control and Moya Moya disease (MD) patients. (a) ULM density map of control patient *n*°1 right temporal window, colormap from 0 to 4.5 (a.u.), (b) ULM density map of control patients *n*°8 left temporal window, colormap from 0 to 5 (a.u.), (c) ULM density map of MD patient *n*°16 left temporal window, colormap from 0 to 3.5 (a.u.), (d) ULM density map of MD patient *n*°18 left temporal window, colormap from 0 to 2.5 (a.u.). (e) Number of localizations per cm² inside perforating arteries' region between MD and control patients, (f) number of tracks per cm² inside perforating arteries' region between MD and control patients, (g) number of at least 8 pixels connected objects (a.u.), *i.e.*, perforating arteries, inside perforating arteries' region between MD and control patients. (h) Mean distance between tracks (px) inside perforating arteries' region between MD and control patients. Same color bar for all patients. White dotted lines indicate perforating arteries' area segmentation. Radiological notation, A, anterior; L, left; P, posterior; R, right. Student *t*-tests were performed to compare the two groups [39].

individualized therapeutic interventions and complement conventional imaging by offering a functional microcirculatory biomarker in coronary and myocardial diseases.

Yan et al. demonstrated the feasibility of transthoracic myocardial ULM in a clinical setting in 4 patients with a programmable research scanner at high frame rate. Only 5 s of the acquisition were used. Using a customized data processing pipeline, they implemented a two-level motion correction approach to minimize the effects of cardiac tissue motion. Intensity-based gating was employed to select frames during the diastolic phase (minimal motion). After differentiating MB signals from tissue signals, a two-step image registration process was used, incorporating singular value decomposition filtering to reduce noise and rigid image registration to align images across cardiac cycles [47,48].

This method enabled the visualization of myocardial microvasculature and highlighted the potential for developing future biomarkers of myocardial microcirculation (Fig. 3) [47].

Kidney

The kidneys are affected by a broad spectrum of conditions, including ischemic injury, drug toxicity, autoimmune disorders, tumors, arterial hypertension and diabetes—conditions in which microcirculation plays a critical role. Microcirculation dysfunction is recognized as one of the earliest indicators of acute kidney injury (AKI) and a key driver of disease progression [49,50]. Glomeruli, the functional units responsible for blood filtration and composition regulation [51], rely heavily on specialized capillary networks, with damage impairing filtration capacity

Table 2
Extracted quantitative and qualitative data

Organ/disease	Paper	Extracted data
Brain	Demené et al. [35]	Transcranial ULM resolution up to 25 μm; depth up to 120 mm; aberration correction increased detected tracks by +5 to 13% (>10 frames) or up to +43% (>30 frames)
	Knieling et al. [36]	Visualization of vascular remodeling post-neuroendovascular treatment in neonates
	Huang et al. [38]	Resolution ~30 μm; differential capillary/large vessel behavior with intracranial pressure
	Denis et al. [39]	Perforating arteries visualized in all subjects; diameter 0.8 ± 0.3 mm (controls); track mean distance differentiates Moya Moya ($p \approx 0.05$)
	Regensburger et al. [37]	First transfontanellar ULM in perinatal stroke
Carotid artery	Goudot et al. [43]	MB detections/s in carotid wall: 121 (80–146) active TA vs. 10 (6–15) quiescent ($p = 0.0005$); path length 43 mm vs. 4 mm; perfusion 3.9 vs. 0.5 mm³/s ($p < 0.001$)
	Goudot et al. [44]	Visualization of vasa vasorum interna in active TA
	Leroy et al. [45]	Plaque neovascularization quantifiable with ULM; density 2.9 ± 1.3 vessels/mm² in vulnerable plaques vs. 0.9 ± 0.4 in stable; correlation with microcalcification ($r = 0.62$, $p < 0.01$)
Heart	Yan et al. [47]	Feasibility of transthoracic ULM; visualization of myocardial microvasculature; 5 s acquisition; successful in 8/10 subjects
Liver	Huang et al. [16]	Greater vessel tortuosity and tapering in diseased liver vs. healthy
Kidney	Huang et al. [16]	Resolution 57.5 μm; motion <15 μm; differentiation of cortical arteries/veins
	Chen et al. [60]	Loss of vasculature in CKD; reduced blood flow and hypoxia hypothesis
	Bodard et al. [61]	Visualization of vessels down to 0.3 mm; smallest analyzable vessel cross-section on ULM: 0.3 ± 0.2 mm; vs. SMI 0.8 ± 0.3 mm, ADF 1.2 ± 0.4 mm, color Doppler 1.3 ± 0.5 mm; maps of interlobar, arcuate, cortical, medullary vessels
	Denis et al. [23]	sULM detects microbubble behavior in glomeruli; quantitative metrics include remanence time and normalized distance; visualization of 5%–10% of glomeruli in allografts
	Bodard et al. [57]	Native kidneys: 16 glomeruli/cm² (6–31); Allografts: 33 glomeruli/cm² (18–55); visualization success 12/15
	Huang et al. [63]	AKI vs. control: TTP 80.3 s vs. 54.2 s; density 18.46 vs. 44.93; RI 0.69 vs. 0.61 ($p < 0.003$)
	Huang et al. [63]	Allograft dysfunction: density 14.6% vs. 31%; flow 13.8 vs. 19.2 mm/s; $p < 0.001$
	Huang et al. [63]	Optimal MB dose and imaging window 1–2 min; tradeoff MB sparsity/SNR
	Grieshaber-Bouyer Mandelbaum et al. [62]	Glomeruli in the renal cortex of neonates using a standard clinical ultrasound device
Testes	Li et al. [72]	Resolution 75 μm; OA vessel diameter 187.4 μm vs. NOA 135.1 μm ($p < 0.001$); vessel density 0.53 vs. 0.39 ($p < 0.01$)
	Li et al. [73]	OA vs. NOA: vessel diameter 183.6 vs. 141.3 μm; density 0.542 vs. 0.392; fractal 1.852 vs. 1.793; correlations with FSH ($r = -0.67$, $p < 0.001$)
Prostate	Solomon et al. [74]	Resolution 220–330 μm
Thyroid	Hansen-Shearer et al. [93]	Partial vascular network assessed in 3D
Tumors		
Breast	Dencks et al. [87]	Feasibility; quantifiable parameters from incomplete vessel trees
	Opacic et al. [88]	HER2+ and TNBC vascular phenotypes; perfusion changes post-chemotherapy
	Morris et al. [76]	Changes in vessel density/diameter/flow entropy post-RT; detection 2 wk vs. RECIST 6 mo
	Huang et al. [16]	Resolution improvement over power Doppler
	Lei et al. [89]	Microvessel density positively correlated with elasticity (SWE)
	Li et al. [90]	Qualitative morphology AUC 0.935 (Sens 94.1%, Spec 92.9%); best quantitative: largest diameter AUC 0.962 (cutoff 763.9 μm; Sens 88.2%, Spec 92.9%)
Liver	Zeng et al. [91]	FNH vs. HCC/LM: higher vessel density, fractal dimension, flow entropy ($p < 0.01$)
Kidney	Bodard et al. [92]	Tumor vs. pseudotumor: glomeruli paths 10 ± 6 vs. 26 ± 5/cm²; dispersity 0.13 vs. 0.3 AU
Prostate	Kanoulas et al. [75]	Excellent correspondence between velocity maps and histopathology. Reasonable spatial agreement between density maps and histologic sections
Lymph node	Zhu et al. [94]	Flow irregularity 60% higher in metastatic vs. reactive LN ($p = 0.0465$)

ADF, advanced dynamic flow; AKI, acute kidney injury; AUC, area under the curve; CKD, chronic kidney disease; FNH, focal nodular hyperplasia; FSH, follicle-stimulating hormone; HCC, hepatocellular carcinoma; HER2, human epidermal growth factor receptor 2; LM, liver metastasis; LN, lymph node; MB, microbubble; NOA, non-obstructive azoospermia; OA, obstructive azoospermia; RI, resistive index; RT, radiotherapy; Sens, sensitivity; SMI, superb microvascular imaging; Spec, specificity; SWE, shear wave elastography; TA, Takayasu arteritis; TNBC, triple-negative breast cancer; TTP, time-to-peak; ULM, ultrasound localization microscopy.

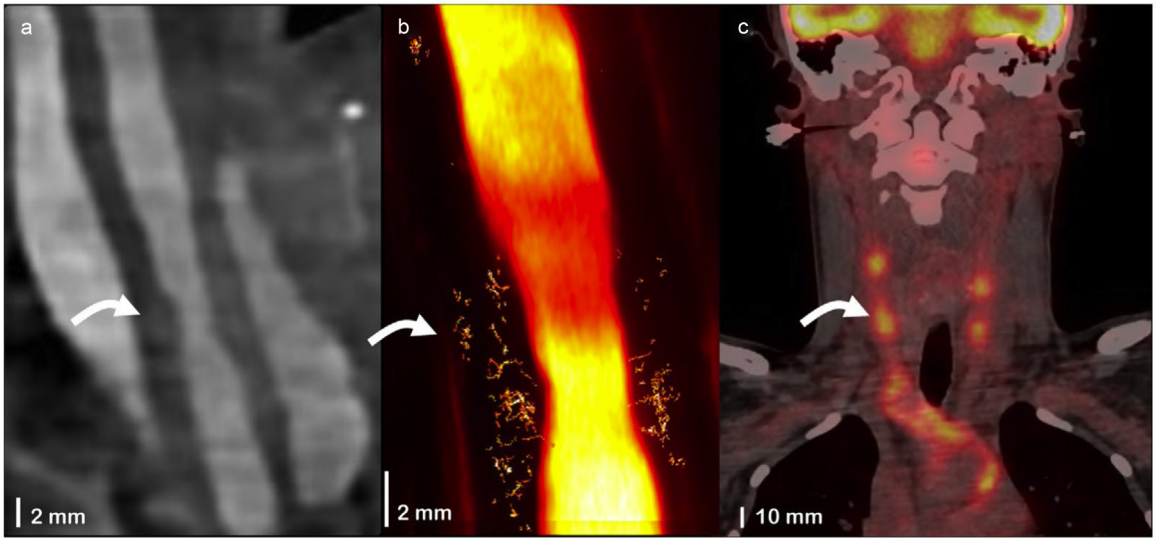

Figure 2. Example of active Takayasu arteritis. CTA reconstruction in frontal view of the right common carotid artery (a). Image at the same site obtained in ULM (obtained from 8-s long acquisition after motion correction) with visualization of microvessels (b). Fluorodeoxyglucose positron emission tomography/computed tomography imaging shows intense fixation localized to the common carotid walls (c) [43].

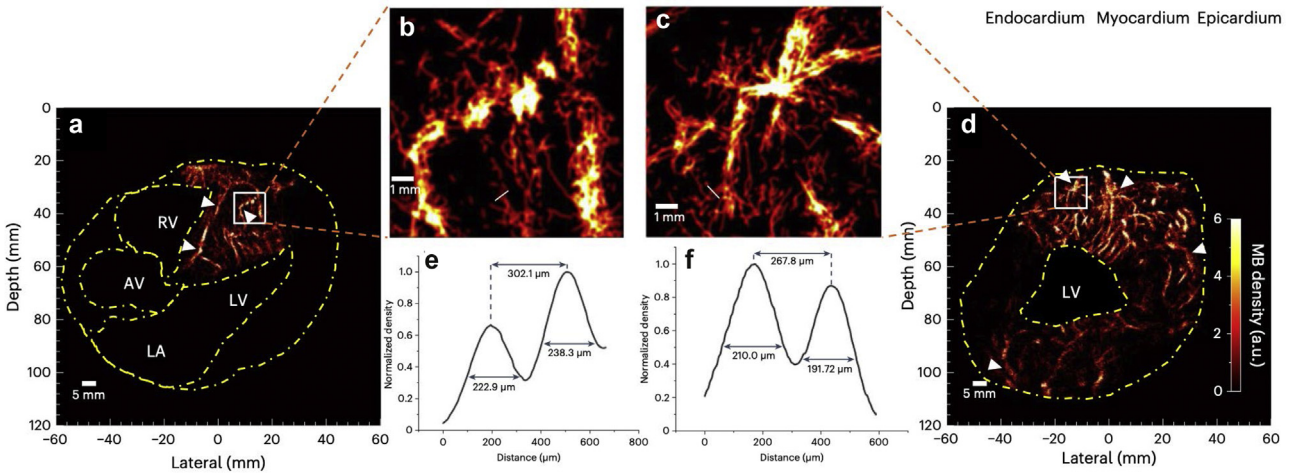

Figure 3. ***In vivo*** **transthoracic myocardial ULM imaging**. (a and d) Myocardial ULM density maps. The yellow dashed lines indicate the chamber regions that were cropped out. (b and c) Zoomed-in density map of white boxes in d and g, white solid lines indicate where the vessel was cut for cross-section analysis. (e and f) The density profile normalized to its maximum from the cross-section analysis [47].

[52–54]. However, the small size of glomeruli (~200 microns) [55,56] renders them invisible to conventional imaging techniques, leaving functional assessment reliant on indirect methods such as blood or urine tests or invasive biopsies [57–59]. ULM provides a unique opportunity to non-invasively visualize renal microvascular networks and even identify individual glomeruli *in vivo*, offering spatially resolved information that previously required histology. Clinically, this approach could enable early detection of microvascular rarefaction in acute and chronic kidney disease, improve graft monitoring without repeated biopsies and support the development of quantitative microvascular biomarkers to guide nephroprotective strategies.

Huang et al. [16] demonstrated that clinically available high-frame-rate US scanners, capable of operating at >500 Hz (compared to 10–15 Hz for conventional systems), can achieve super-resolution microvascular visualization within a relatively short acquisition time (6.0–9.7 s). They achieved a spatial resolution of 57.5 μm, reduced residual tissue motion to <15 μm, and could distinguish individual MBs with opposite flow directions in the arteries and veins of the cortex.

Recently, Chen et al. used available high-frame-rate US scanners to compare blood vessels of native human kidneys in normal and disease states. They demonstrated loss of kidney vasculature in chronic kidney disease, a phenomenon shown repeatedly in animal models of disease. Reduced blood flow could subject the kidney to chronic hypoxia and promote further injury [60]. SRUS provides unique data on vascular structure that could aid in our understanding and treatment of kidney disease.

Quantitative microvascular analysis in kidney grafts was performed by refining post-processing methods of image obtained using a commercially available clinical US system at low frame rate [61]. This study generated ULM-derived density maps that revealed interlobar, arcuate, cortical radial vessels and portions of the medullary structure. A mean smallest imageable vessel diameter of 0.3 mm was achieved, compared with superb microvascular imaging (0.8 mm), advanced dynamic flow (1.2 mm) and color Doppler (1.3 mm). These findings highlighted ULM's potential as a non-invasive imaging tool for identifying kidney disease biomarkers using standard clinical equipment, paving the way for expanded clinical research (Fig. 4) [61].

Building on this work, "sensing ULM" (sULM), a novel technique classifying MB motion patterns was introduced [23]. This advancement enabled the first *in vivo* visualization of approximately 5%–10% of

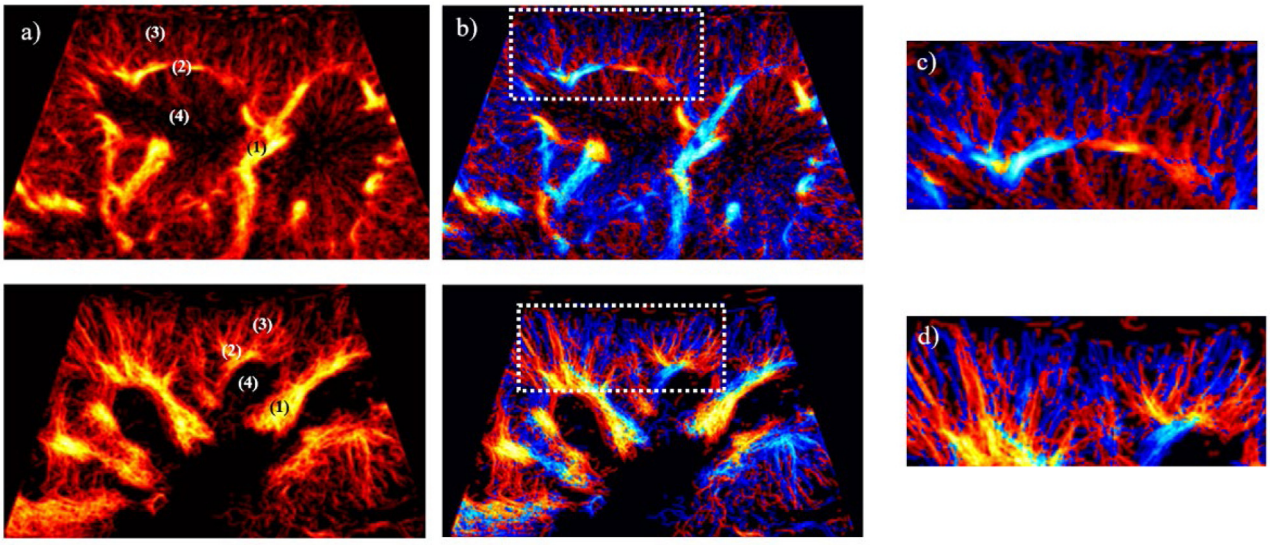

Figure 4. ULM of kidney grafts. (a) ULM density maps in two patients highlight interlobar arteries (1), arcuate arteries (2), cortical radiate arteries (3) and part of medullar organization (4). (b) ULM directivity maps in two patients. (c and d) Close-up of the two patients' ULM directivity maps [61].

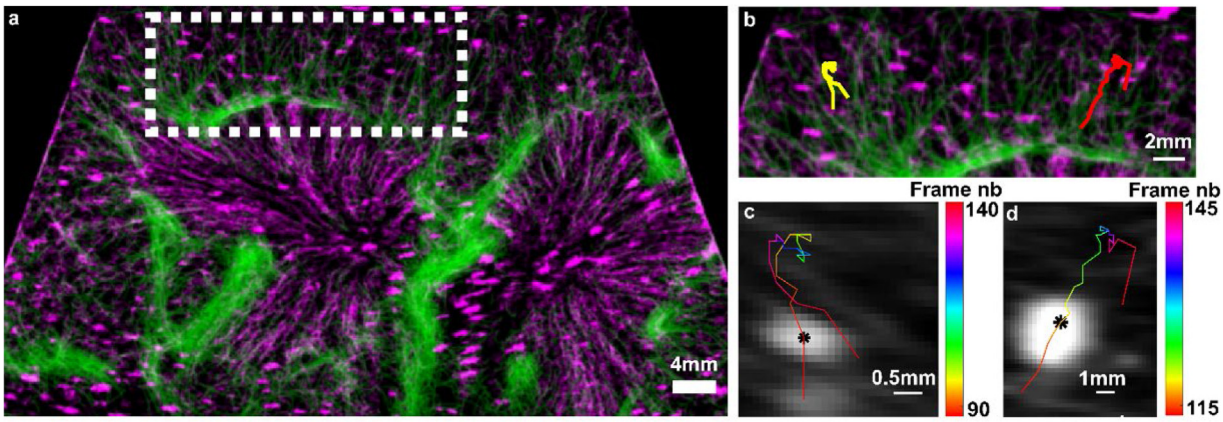

Figure 5. Glomeruli observed in the cortex of human kidneys by sULM. (a) sULM density map in patient one with superimposed slow-tracking (pink) and fast-tracking (green). (b) Zoom in the cortex area. (c) Zoom of yellow track highlighted in part (b). (d) Zoom of red track highlighted in part (b) [23].

kidney glomeruli in allografts. sULM's spatial coverage far exceeded that of biopsy, potentially reducing sampling errors in kidney assessments (Fig. 5) [23]. Grieshaber-Bouyer Mandelbaum et al. [62] further validated this technique in the kidneys of 5 neonates.

Further validation of sULM was conducted in native kidneys, where imaging is more challenging due to greater depth and limited accessibility. In these cases, imaging duration was constrained by the patient's breath-holding capacity to minimize motion artifacts, reducing the data acquisition volume. Native kidneys, with an average depth of 98 mm compared to 36 mm for grafts, exhibited fewer MB tracks (mean 148/cm^2 in native kidneys vs. 679/cm^2 in allografts) and fewer detected glomeruli for the same acquisition time (16/cm^2 in native kidneys vs. 33/cm^2 in allografts), highlighting depth-related limitations (Fig. 6) [57].

Huang et al. [63] explored ULM's utility in AKI, reporting increased renal cortex transit times (80.3 s in AKI vs. 54.2 s in controls, $p < 0.001$), reduced microvascular density (18.46 in AKI vs. 44.93 in controls, $p < 0.001$) and altered perfusion (renal interlobar flow resistance index of 0.69 in AKI vs. 0.61 in controls, $p = 0.003$). Microvascular density reduction, potentially reflecting neutrophil infiltration and microvascular embolism [64], correlated negatively with serum creatinine levels and aligned with other biochemical markers, including urine output and glomerular filtration rate.

Huang et al. observed significant decreases in microvascular density (31% in patients with normal allografts vs. 14.6% in those with allograft dysfunction) and microvascular flow rates (19.2 mm/s vs. 13.8 mm/s, both $p < 0.001$). They proposed combining ULM-derived microvascular density

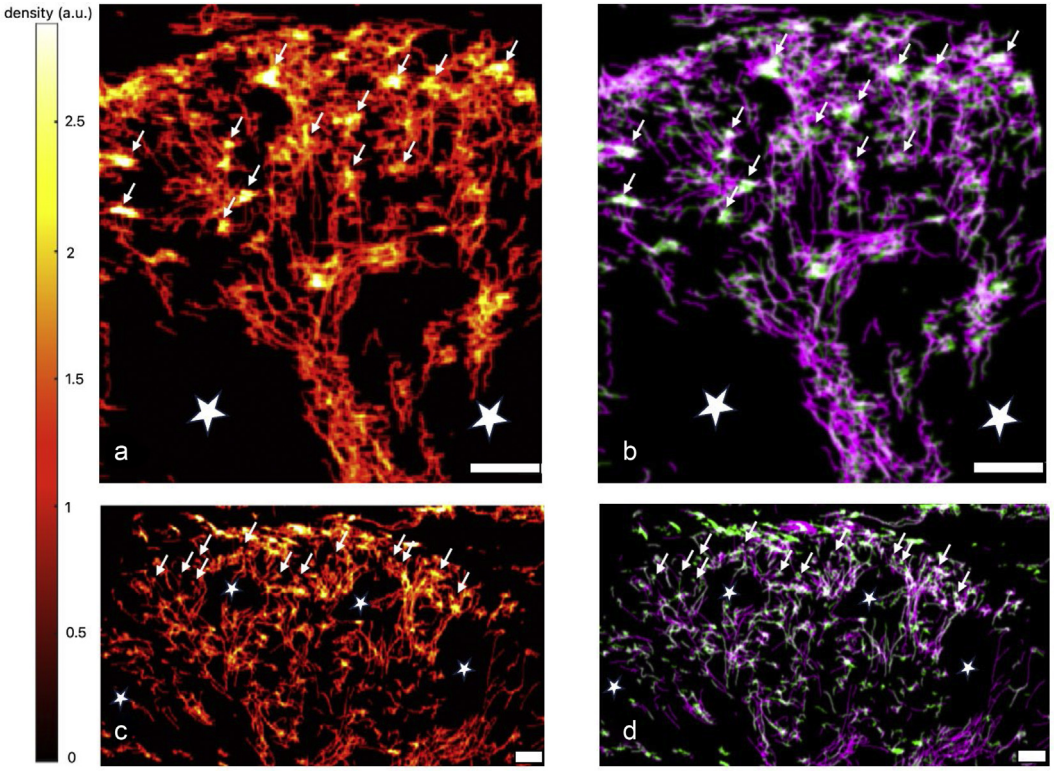

Figure 6. Composite density maps of two native kidneys. Composite density in two native kidneys (a and c). Treatment and color representation enhance the visibility of glomeruli with slow microbubbles in green and fast ones in pink (b and d). Scale bars indicated 4 mm. The arrows show examples of glomeruli. The stars show the medulla [57].

with CEUS time-to-peak measurements as a novel biomarker for renal allograft dysfunction, refining the selection of patients requiring biopsy [63].

Finally, Huang et al. studied the optimum criteria for consistent and reproducible ULM. They showed that optimizing ULM in humans requires balancing MB sparsity, count and signal-to-noise ratio, with an optimal imaging window of 1−2 min during the wash-out phase. Higher MB doses delay peak concentration and extend the wash-out phase, but can impair localization due to overlap. Increased acoustic power enhances MB signal and penetration but risks MB destruction in later phases [65].

Testes

Azoospermia, a major cause of infertility affecting ~1% of men, is classified as either non-obstructive (NOA) or obstructive azoospermia (OA) [66,67]. The gold standard for diagnosis is biopsy, which carries risks of unintended tissue damage that may further impair fertility [68,69]. Teste microcirculation is closely linked to spermatogenic function and holds diagnostic potential [70,71]. ULM enables detailed mapping of testicular microvasculature and quantification of flow patterns, providing functional insights that correlate with spermatogenic activity. Clinically, it could offer a non-invasive alternative to biopsy for distinguishing obstructive from NOA, monitor treatment response and improve fertility preservation by identifying patients who may still benefit from sperm retrieval procedures.

Li et al. achieved detailed mapping of testicular microvascular architecture in 76 infertile NOA and OA patients compared to 15 controls with a resolution of 75 μm and blood vessel separation of 81 μm using regular frame-rate clinical US. They assessed parameters such as tortuosity, vascular density, branching patterns and blood flow connectivity. Mean vessel diameter emerged as a promising biomarker for differentiating azoospermia types, with larger mean vessel diameters observed in OA (187.4 μm) compared to NOA patients (135.1 μm). The study proposed a negative feedback loop in sperm production as a potential biological mechanism for these vascular differences, though it was not histologically confirmed [72].

In a subsequent paper, Li et al. explored pressure distribution mapping derived from velocity distribution data. NOA patients exhibited uneven pressure distribution, with areas of low pressure correlating to sparse blood perfusion and reduced vascular density—both linked to impaired fertility. In contrast, OA patients displayed more uniform vascular pressure distributions, indicating better-preserved microvascular function. They also revealed increased mean vessel diameter, vascular density and fractal number in OA (183.6 μm, 0.542, 1.852) compared to NOA (141.3 μm, 0.392, 1.793). These findings suggest a more robust vascular network in OA, potentially as a compensatory mechanism in response to reproductive tract obstruction [73].

This study further established a direct connection between testicular microvasculature and spermatogenic function. Key hormones regulating testicular function, such as follicle-stimulating hormone (FSH) and luteinizing hormone, negatively correlated with mean vessel diameter and velocity. The authors proposed a combined diagnostic model integrating clinical parameters (*e.g.*, FSH levels) and vascular biomarkers (*e.g.*, mean diameter) to assess testicular function comprehensively (Fig. 7) [73].

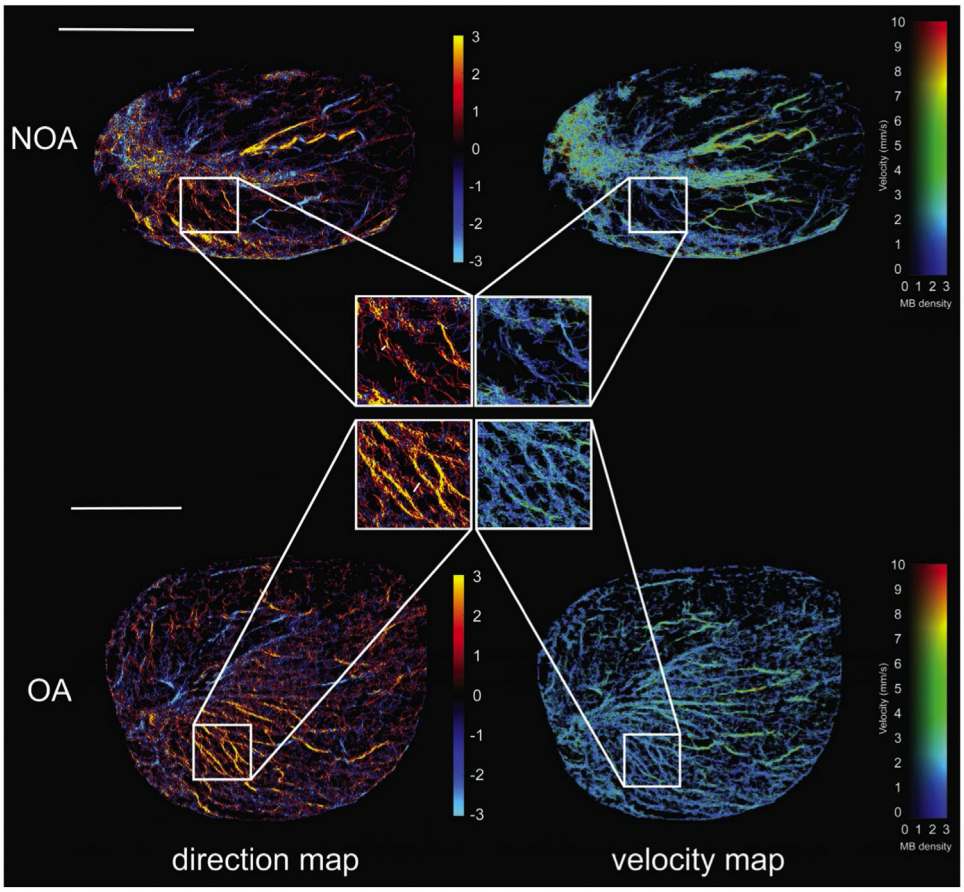

Figure 7. ULM of testicular microvasculature in patients with non-obstructive azoospermia (NOA) and obstructive azoospermia (OA). The top panel represents NOA, and the bottom panel represents OA. Each panel includes a direction map on the left, displaying the orientation of blood flow (red indicates microbubble flow toward the transducer, while blue signifies flow away from the transducer) and a velocity map on the right, showing the speed of blood flow within the testicular tissue. Highlighted regions of interest within white boxes were magnified to provide a closer view of each condition's vascular patterns and flow dynamics characteristic. MB, microbubble. Scale bars = 1 cm [72].

Other organs

Huang et al. [16] used clinically available high-frame-rate US scanners to reveal greater tortuosity of vessels in the diseased liver compared to a healthy liver and tapering in the main branches, suggesting pathological changes to the liver tissue.

Solomon et al. demonstrated advances in super-resolution imaging (SRI) in the prostate. They employed a novel method, 3SAT, which uses weighted sparse recovery minimization combined with online tracking of individual MBs, resulting in a resolution of around 220–330 μm. This improved algorithm was applied to data from a human prostate, enhancing the detection rates of MBs and improving motion tracking, which enabled the extraction of more detailed quantitative information on microvascular structure and hemodynamics. Real-time processing could improve ULM in clinical practice by allowing better probe positioning and facilitating the detection of small pathologies. However, the findings were based on data from a single patient, highlighting the need for further research and validation in larger cohorts to confirm the method's clinical applicability [74].

Finally, a recent 3-D transcutaneous study using a row–column array demonstrated *in vivo* feasibility on the human thyroid, after introducing a coherence-based beamforming and rolling sub-aperture processing that reduced false localizations from ~26% to ~15%, improved signal/noise ratio by ~7 dB, and raised the effective frame rate to >4000 frame/s. These advances enabled non-invasive super-resolution mapping of thyroid microvasculature with markedly fewer artefacts, supporting the clinical potential of ULM for superficial endocrine organs [75].

Oncology

CT and MRI remain the standard imaging modalities for monitoring tumor size based on response evaluation criteria in solid tumors (RECIST) criteria [76]. However, these techniques fail to capture the complexity and heterogeneity of tumors [77] or the earliest biological changes in response to treatment [78]. Pathological angiogenesis, a hallmark of cancer [5], drives the development of tortuous and irregular microvascular structures [79–81], contributing to regional hypoxia and therapy resistance [82].

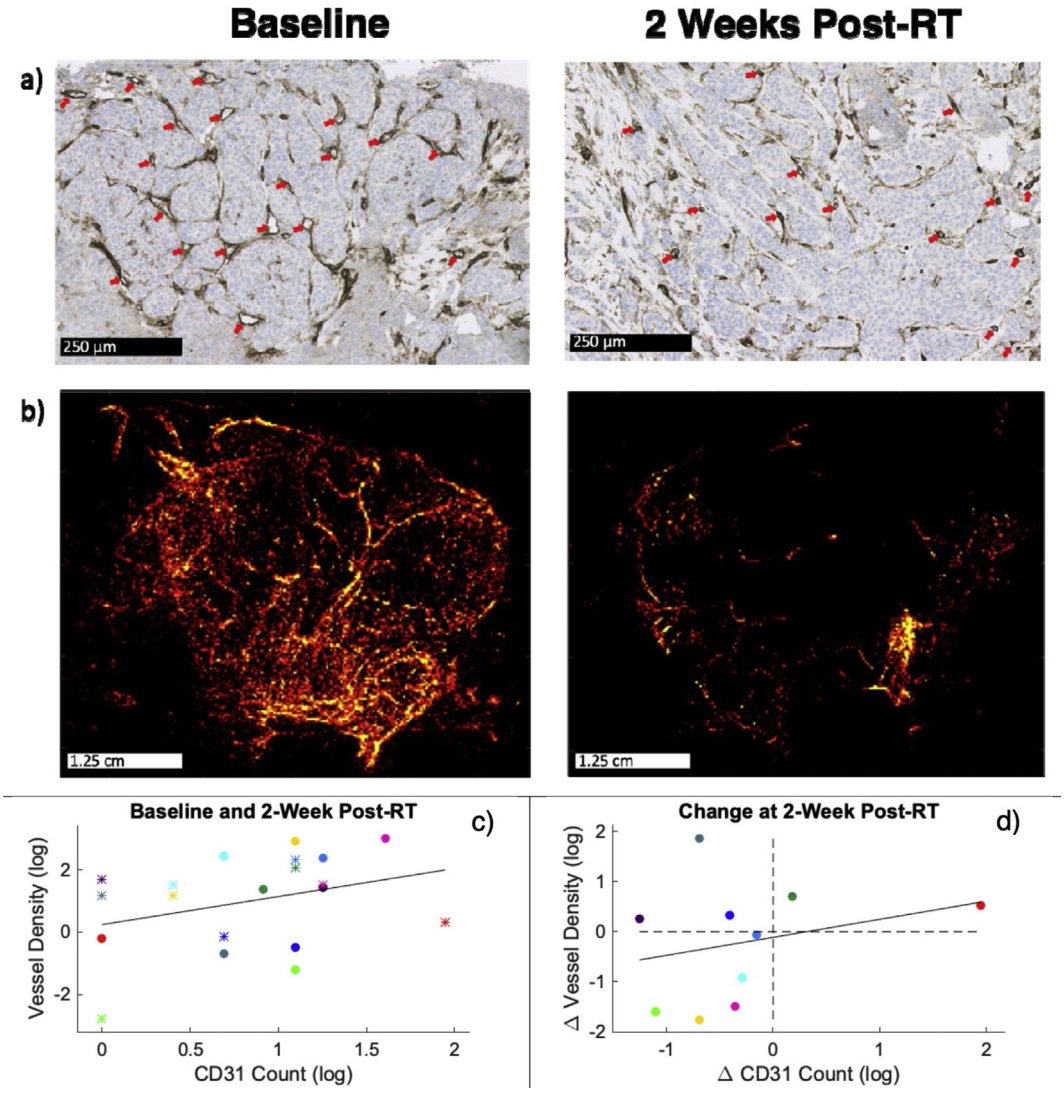

Figure 8. ULM of breast tumors before and post-radiotherapy. (a) Breast core tumor biopsy section from a participant stained for CD31 (endothelial cell marker) at baseline (left) and 2 wk post-radiotherapy (right) showing a clear reduction in blood vessels. Some blood vessel examples are highlighted with red arrows; the stained vessel lumens generally appear smaller post-radiotherapy treatment. (b) Super-resolution ultrasound (SRUS) images from the same participant at baseline (left) and 2 wk post-radiotherapy (right). (c) Plot of the absolute values of the natural logarithm of the SRUS vessel density and CD31 count (as scored by a histopathologist) for 10 participants pre-radiotherapy and 2-wk post-radiotherapy, with the black line being a line of best fit. (d) Plot of the change in the SRUS vessel density and CD31 count at 2 wk post-RT for 10 participants. The black line is the line of best fit, and the dashed black lines represent zero change. The colors signify the participants [74].

These features make angiogenesis a promising target for developing biomarkers for early detection, prognosis, therapy selection, therapeutic response monitoring [80] and early identification of non-responders [83–86]. ULM offers the ability to resolve and quantify tumor microvascular architecture and dynamics at the capillary scale, enabling direct assessment of angiogenic activity and perfusion heterogeneity. Clinically, this could provide early biomarkers of therapeutic response, complement or surpass RECIST-based assessments by revealing functional changes before size reduction, and help tailor anti-angiogenic or radiotherapy (RT) strategies to individual tumor biology. a. Breast tumors

In a pioneering study, Dencks et al. shown that clinical SRI is feasible with a single contrast agent injection within measurement times of less than 5 min. Although vessel trees were not imaged completely with the statistical sampling by the MBs, relevant parameters could be derived also from incomplete vessel trees by investigating their reconstruction over time [87]. The same year, Opacic et al. demonstrated the ability to identify tumors based on their vascular phenotype in animal models. They used longer measurement times (approximately 40 s) and achieved a spatial resolution of 10 μm. As a clinical proof-of-concept, they extended this approach to the tumors of three cancer patients. In their clinical findings, a HER2-positive breast cancer patient exhibited a vascular pedicle, with a dense network of feeding and draining vessels in the lower part of the tumor and homogeneous vascularization throughout the tissue, albeit with increased vascularization on one side. A second patient with triple-negative breast cancer (TNBC) demonstrated increased vascularization following the first chemotherapy administration, with relative blood volume rising from 0.04% to 1.8% despite a reduction in tumor volume. This high vascularization persisted with a further decrease in tumor volume after a second dose of chemotherapy. Enhanced peripheral vascularization was observed in another TNBC patient following the first and second chemotherapy cycles, with increased relative blood volume despite tumor volume decreasing from 25.6 cm^3 to 3.0 cm^3 and then to 0.8 cm^3 [88].

Morris et al. further demonstrated the utility of multi-plane SRUS in assessing microvascular changes in a study involving 24 repeatability scans on 11 patients post-RT. Sensitive and repeatable biomarkers revealed heterogeneous microvascular responses to RT, including vessel density, diameter, blood flow speed and local blood flow direction entropy. Significant changes were observed in half of the patients within 2 wk of treatment, compared to only one detected using RECIST criteria. By 6 mo, all participants showed significant changes in at least one ULM parameter, whereas only 6 patients demonstrated changes with RECIST criteria [76]. A comparison with histopathological vessel count scores showed agreement in 70% of patients, with both methods indicating the same directional changes. However, while histological CD31 staining detects both functional and non-functional vessels, ULM uniquely identifies only functional vessels with active

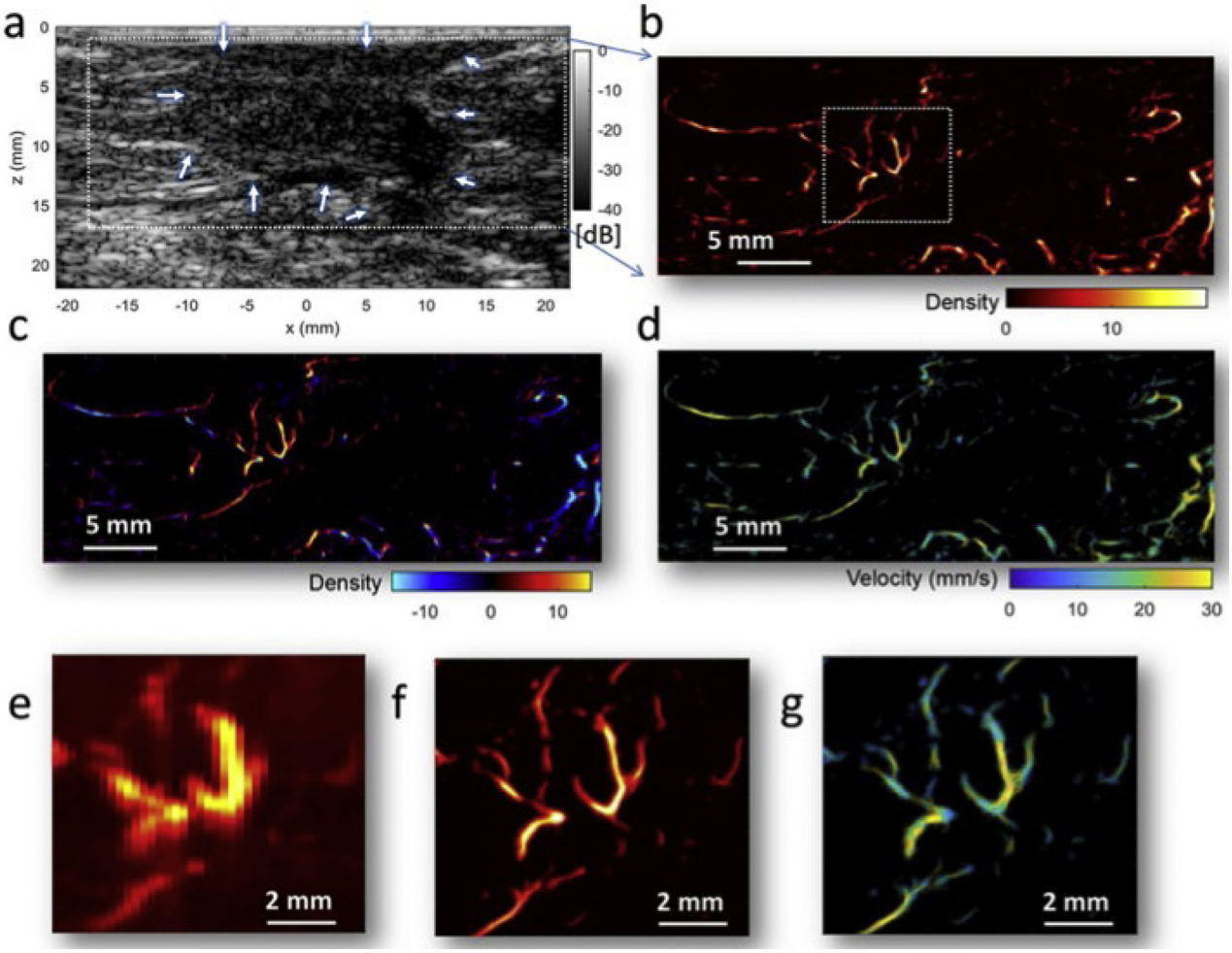

Figure 9. ULM of breast tumor with high-frame-rate ultrasound scanners. (a) B-mode image of a breast tumor diagnosed as ductal carcinoma in situ from a 49-y-old patient after neoadjuvant chemotherapies, with white arrows roughly indicating the boundary of the lesion. (b) Corresponding super-resolution microvessel density image of the human breast tumor. (c) The corresponding bi-directional microvessel density image is similar to part (b), but with red color indicating the upward flow and blue color representing the downward flow. (d) Corresponding super-resolution microvessel velocity image, with colormap indicating the magnitude of the velocity. (e) Zoom-in region (indicated by the white rectangle in part [b]) of the contrast-enhanced power Doppler image. (f) Corresponding zoom-in region of the super-resolution microvessel density image. (g) Corresponding zoom in the region of the super-resolution microvessel velocity image [16].

blood flow. This highlights ULM's potential to provide more precise and clinically relevant insights into tumor microvascular function (Fig. 8).

Moreover, Huang et al. [16] analyzed a breast tumor with clinically available high-frame-rate US scanners at a depth of 15 mm and demonstrated a substantial improvement in resolution compared to power Doppler (Fig. 9).

Furthermore, Lei et al. evaluated the correlation between the elastic modulus, assessed using shear-wave elastography (SWE) and microvascular characteristics captured through SRUS, in order to evaluate the effectiveness of combining these techniques in distinguishing between benign and malignant breast masses. They demonstrated that the microvessel density of the breast mass shows a significant positive correlation with maximum elasticity. By integrating SRUS with SWE, they propose a novel diagnostic approach designed to improve specificity and accuracy in breast cancer detection [89]. This approach shows promise for early breast cancer detection, with the potential to reduce the need for unnecessary biopsies and improve patient outcomes.

Finally, a prospective, multicenter clinical trial involving 83 patients has been launched to evaluate the role of ULM in differentiating benign from malignant breast tumors and predicting histologic biomarkers associated with prognosis. The protocol for this study, which aims to explore both qualitative and quantitative ULM parameters, has been published and registered under the Chinese Clinical Trial Registry (ChiCTR2100048361) [90]. b. Pancreatic tumor

Huang et al. tested ULM using clinical high-frame-rate scanners to evaluate a large pancreatic tumor at a depth of 60 mm. They successfully differentiated feeding and draining vessels, providing detailed morphological and hemodynamic characteristics with high resolution (Fig. 10) [16]. c. Liver tumor

Zeng et al. used a high frame rate (350−500 Hz) modified US scanner to perform ULM of 47 focal liver lesions (FLL), including 30 hepatocellular carcinomas (HCC), 11 liver metastases (LM) and 6 focal nodular hyperplasias (FNH). They observed higher vessel density for FNH versus liver parenchyma ($p < 0.001$) as well as fractal dimension and local flow direction entropy value for FNH versus HCC ($p = 0.002$ and $p < 0.001$, respectively) and for FNH versus LM ($p = 0.006$ and $p = 0.002$, respectively). They concluded that multiparametric SR-US (vessel density, fractal dimension and local flow direction entropy) could serve as valuable parameters in distinguishing between benign and malignant FLLs [91]. d. Renal tumor

Recently, it was demonstrated that sULM can effectively differentiate renal tumors from renal pseudotumors (healthy tissue) based on the presence or absence of glomeruli [92]. Fewer glomeruli paths were observed in renal tumors (artifacts) compared to either pseudotumors or the kidney cortex (10 ± 6/cm^2 vs. 26 ± 5/cm^2 and 26 ± 6/cm^2,

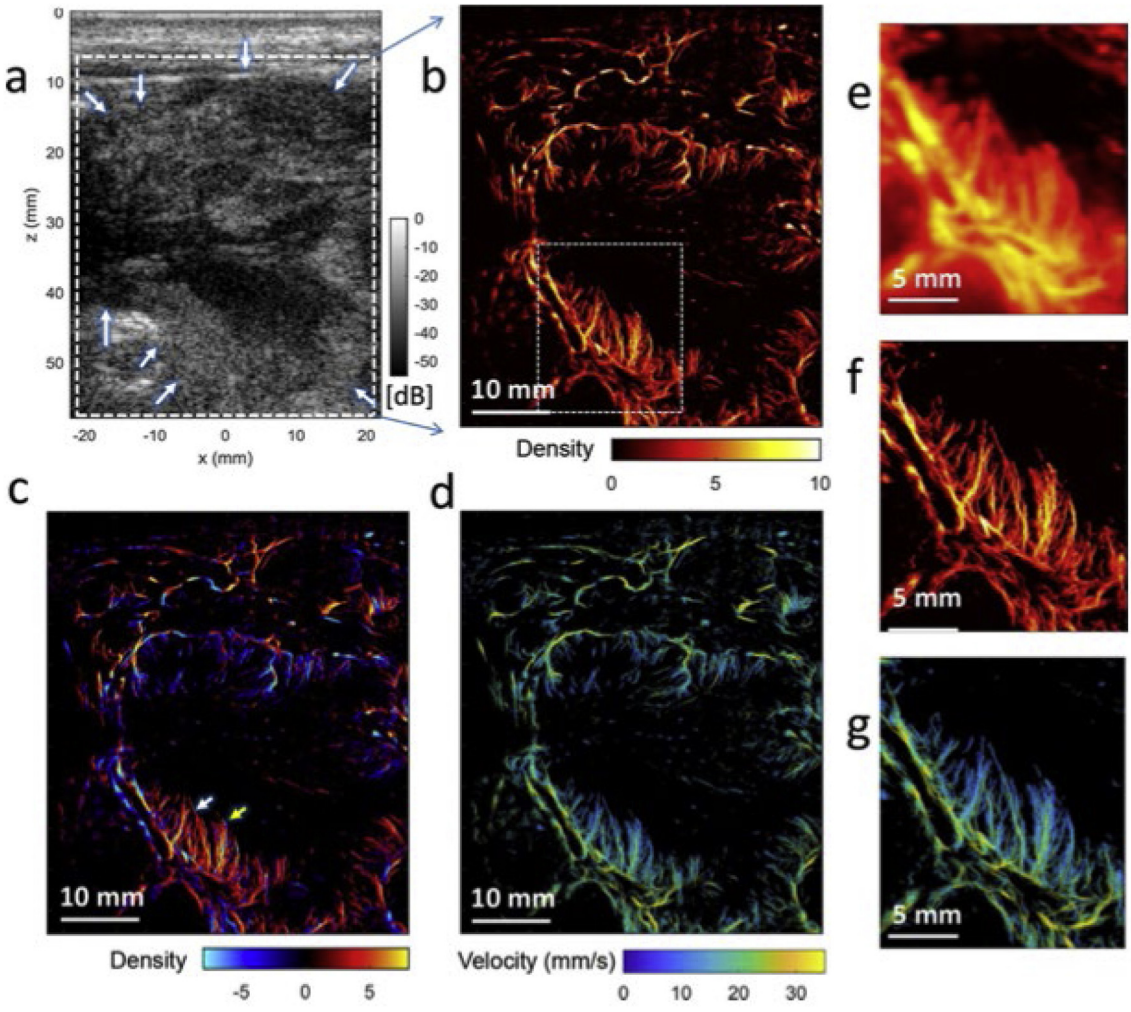

Figure 10. ULM of a large pancreatic tumor using high-frame-rate scanners. (a) B-mode image of a pancreatic tumor from a 70-y-old patient, with white arrows roughly indicating the boundary of the lesion. (b) Super-resolution microvessel density image of the human pancreatic tumor. (c) The corresponding bi-directional microvessel density image is similar to part (b), but with red indicating the upward flow and blue representing the downward flow. (d) Corresponding super-resolution microvessel velocity image, with colormap indicating the magnitude of the velocity. (e) Zoom-in region (indicated by the white rectangle in part [b]) of the contrast-enhanced power Doppler image. (f) Corresponding zoom-in region of the super-resolution microvessel density image. (g) Corresponding zoom-in region of the super-resolution microvessel velocity image [16].

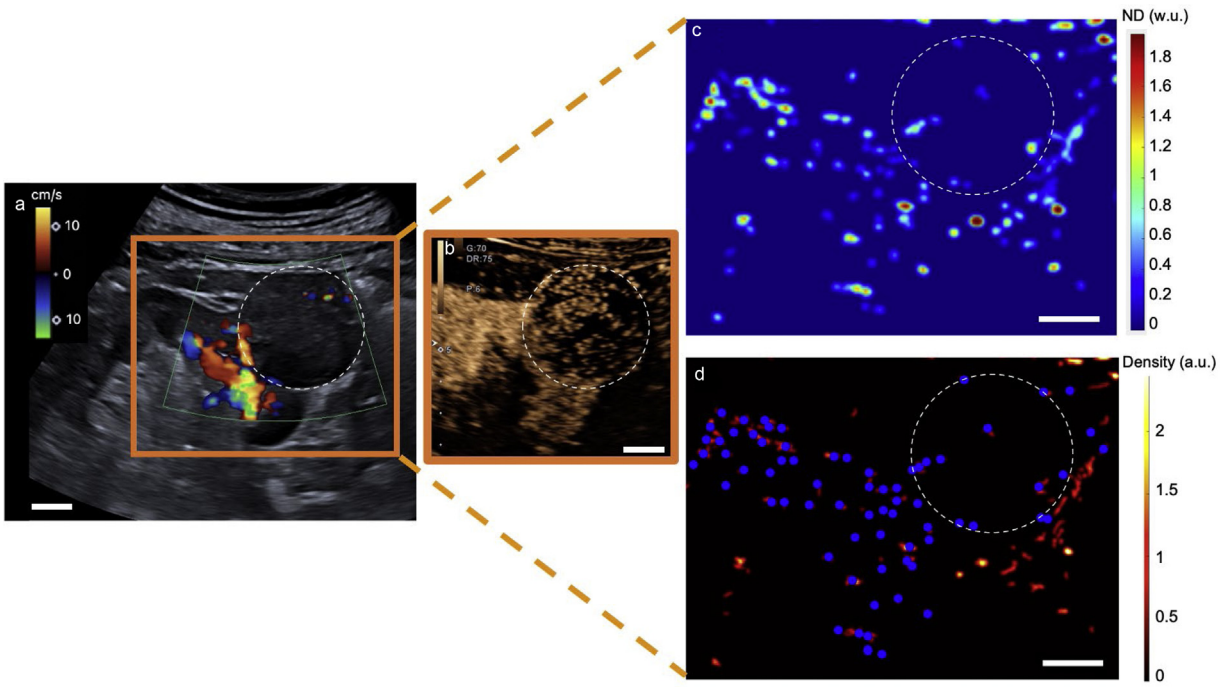

Figure 11. sULM of clear cell renal cell carcinoma (ccRCC). (a and b) Ultrasound Doppler image (a) and CEUS (b) showing an exophytic renal tumor (ccRCC) (white-dotted area). Parts (c and d) show normalized distance metrics. (c) This metric enhances glomerular behavior, highlighting the detected glomeruli in blue points on the density map; (d) note the presence of glomerular paths in the renal cortex and some artifacts mimicking glomeruli in the renal tumor (the image displays the traces projected on the grid in red. The colorbar corresponds to the count of the number of bubbles per pixel. Scale bars indicate 10 mm. a.u., arbitrary units; ND, normalized distance; w.u., without units) [90].

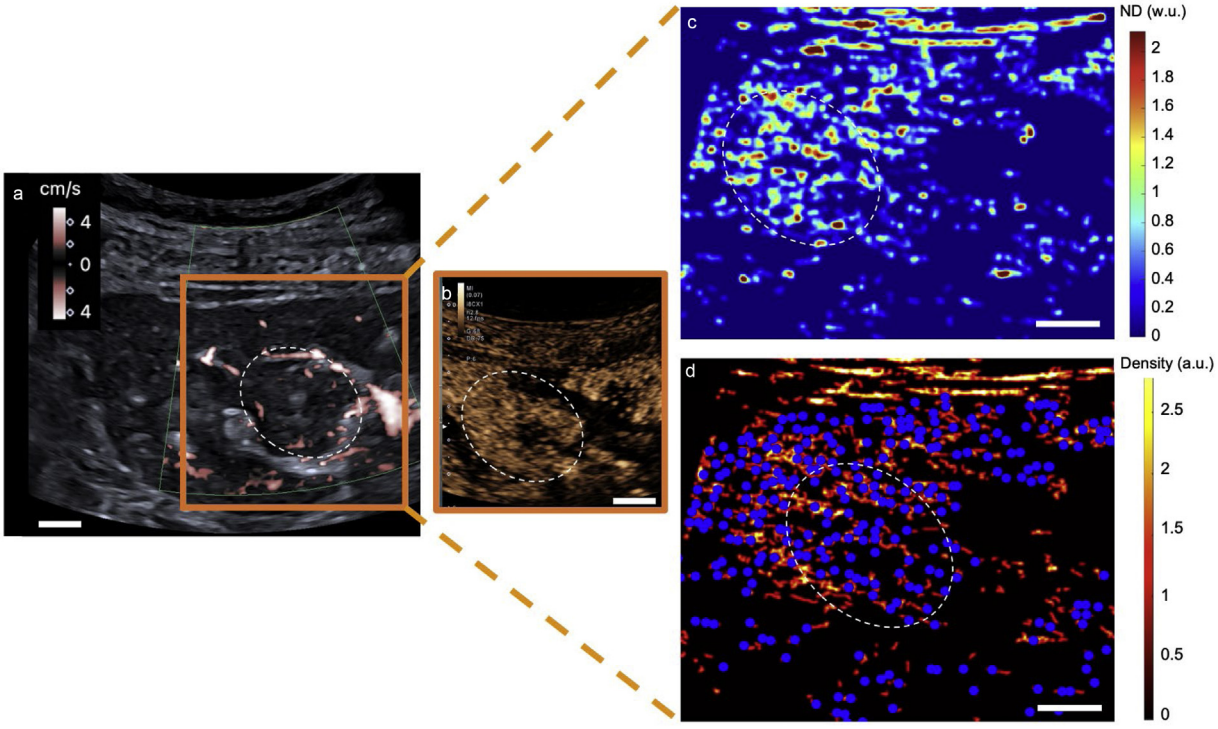

Figure 12. sULM of hypertrophy of the column of Bertin. (a and b) Superb microvascular imaging Doppler image (a) and CEUS (b) showing an endophytic renal pseudotumor (hypertrophy of column of Bertin) (white-dotted area). Parts (c and d) show normalized distance metrics. (c) This metric enhances glomerular behavior, highlighting the detected glomeruli in blue points on the density map. (d) Note the presence of glomerular paths in the renal cortex and the pseudotumor (the image displays the traces projected on the grid in red. The colorbar corresponds to the count of the number of bubbles per pixel. Scale bars indicate 10 mm. a.u., arbitrary units; ND, normalized distance; w.u., without units) [90].

respectively, $p < 0.001$). Dispersity was also lower in renal tumors compared to the cortex or pseudotumor (0.13 ± 0.06 arbitrary units [AU] vs. 0.3 ± 0.1 AU in the cortex and 0.22 ± 0.05 AU in pseudotumors; $p = 0.0012$ and $p = 0.0389$, respectively) as well as normalized speeds (0.08 ± 0.04 vs. 0.18 ± 0.07 in the renal cortex and 0.14 ± 0.02 in pseudotumors; $p = 0.0014$ and $p = 0.0497$, respectively (Figs. 11 and 12). e. Prostatic tumor

In that context, Kanoulas et al. demonstrated that SRUS imaging could visualize intraprostatic microvascular networks with high fidelity. The velocity maps showed an excellent correspondence with histopathology, while the density maps also displayed reasonable spatial agreement with histologic sections. This proof-of-concept study confirmed the feasibility of resolving the microvascular architecture and quantifying local hemodynamics within the prostate, suggesting potential clinical utility for characterizing tumor angiogenesis and differentiating malignant from benign regions [93]. f. Lymph node

Distinguishing metastatic lymph nodes (LNs) from benign lymphadenopathy is crucial in cancer management but remains challenging. Zhu et al. conducted a pilot study demonstrating the feasibility of using ULM quantitative markers to address this challenge with a clinical US scanner. The study identified differences in flow irregularity between reactive and metastatic LNs. Specifically, local flow direction irregularity—a marker of disorganized blood flow—was observed to be 60% higher in metastatic LNs (1600) compared to reactive LNs (1000) ($p = 0.0465$). This finding was consistent across various malignancy types and locations [94]. However, other parameters, including vessel density, flow direction, spatial complexity and flow velocity, did not yield statistically significant differences.

Discussion

ULM is rapidly advancing and appears poised for clinical translation. However, despite its potential, few biomarkers have been identified, and those suggested as promising targets require robust validation against current gold-standard tests. Repeatability within the same operator has shown promising results, but multi-center studies are necessary to evaluate reproducibility across protocols and assess inter-test variability [76]. Most existing clinical ULM studies remain exploratory, with limited sample sizes and heterogeneous imaging protocols. Comparative studies across organs are scarce, and few have correlated ULM-derived biomarkers with established clinical endpoints such as histopathology, functional tests or patient outcomes. Strengthening these methodological aspects will be essential to move from proof-of-concept to clinically validated applications.

ULM biomarker identification and validation face several limitations. First, conventional clinical US scanners operate at lower imaging frame rates (2–20 Hz) compared to high-frequency research systems, which restricts the ability to track individual MBs [61]. Although sophisticated tracking algorithms can partially address this issue [22], these solutions are not universally effective. To compensate for the low frame rates, acquisition times must be extended to seconds or even minutes, making them highly susceptible to motion artifacts [95–97]. These artifacts stem from hand-held probes and natural tissue movements, such as breathing, pulsatility and local deformations.

While breath-holding is often employed to minimize motion, it limits acquisition duration and poses challenges in regions with significant motion, such as the heart [47] or chest wall [98]. Although motion correction algorithms have shown promise in mitigating these artifacts, limited acquisition time can result in incomplete MB traversal through all microvessels [43], particularly in slow-flowing capillary networks [13,99]. This limitation is more pronounced in specific tissues, such as the liver and kidneys, where blood flow is approximately 10–20 times faster than in the capillary networks. Low vascular saturation further complicates imaging by blurring distinctions between smaller, distinct vessels and larger vessels with overlapping tracks [47].

A two-stage motion correction method combining affine and non-rigid estimations has been developed to address both global motion and local tissue deformation. This approach, tested on clinical US scanners, demonstrated a worst-case error of 12.2 μm [100]. When applied to clinical datasets, the technique effectively reduced motion-induced blurring, narrowing the width of identified microvessels by 1.5-fold, straightening tortuous vessels, removing blurred artifacts and resolving artificial double vessel copies into single representations [100].

Out-of-plane motion presents additional challenges in 2D imaging [101]. MBs moving outside the imaging plane can result in incomplete or inaccurate data [57]. Studies have reported a high rate of data exclusion due to this issue, with Huang et al., Porte et al. and Zhu et al. excluding significant portions of their datasets (3/7 patients, 4/11, 34/44, respectively) due to out-of-place motion, insufficient MB detection or poor signal-to-noise ratios [16,94,96]. Multi-plane imaging can mitigate these challenges. Morris et al. [76] demonstrated that averaging quantitative parameters across multiple planes improved repeatability and robustness, with decreased repeatability coefficients as the number of imaging planes increased (22%–27%, 36%–42% and 42%–48% for 2, 3 and 4 imaging planes, respectively).

Transcranial ULM faces unique challenges due to its limited acoustic window, which is present in only about 20% of patients [102]. Demené et al. addressed this by applying adaptive speckle tracking to correct wave aberrations, showing potential for overcoming this limitation [35,103,104].

Standardization is also required for the administration and dose of MBs [65]. Studies like Porte et al. [98] highlighted the impact of injection parameters on imaging quality. Faster injection speeds (100 vs. 50 μL/s) and higher doses improved vascular reconstructions in slow-flow regions, such as breast tumors. These findings underscore the need for tailored protocols to accommodate regional blood flow differences. Additionally, correlations between vascular density and tumor elasticity, as measured by shear wave elastography, suggest complementary insights into tumor biology ($R = 0.55$, $p = 0.10$ at lower doses; $R = 0.66$, $p = 0.04$ at higher doses).

Beyond technical optimization, future research should focus on disease-specific applications where ULM could offer clear clinical benefit—such as early detection of microvascular rarefaction in diabetic nephropathy, monitoring of tumor response to anti-angiogenic therapies, or evaluation of cerebral perfusion in vascular dementia. Integrating ULM into multimodal diagnostic workflows could enhance precision medicine by adding a functional microcirculatory dimension to conventional imaging.

The translation of ULM into clinical practice will also depend on regulatory and practical factors, including reproducible quantitative outputs, automated data analysis pipelines and integration into existing clinical US platforms. Establishing consensus-driven standards for acquisition, processing and reporting will be crucial to ensure inter-center comparability and facilitate multicenter clinical trials.

The advent of higher frame-rate clinical scanners would improve imaging resolution and reduce acquisition times, although their current availability is limited. 3D ULM represents a transformative opportunity [105–108]. Allowing MB tracking across entire vascular networks and enabling motion correction in all directions [97,105,109]. This advancement would facilitate longer acquisitions without reliance on breath-holding, improve vascular saturation and provide more comprehensive microvascular mapping [22]. However, implementing 3D ULM requires upgraded clinical equipment, increased processing power and enhanced data storage.

Conclusion

ULM has reached a level of technical maturity that enables its reliable use in human clinical settings, providing unprecedented access to microvascular structures and hemodynamics. While the technique itself is ready for clinical implementation, its true clinical translation will

depend on the identification and validation of quantitative biomarkers with diagnostic, prognostic or therapeutic value. Future advancements —including higher frame-rate US systems, real-time processing and 3D imaging—will further enhance its feasibility and reproducibility. The involvement of clinical radiologists in routine applications will be crucial to refine its indications and establish ULM as a valuable tool in precision imaging.

Conflict of interest

O.C. holds patents in the field of ultrasound localization microscopy (EP4011299A1). O.C. is one founder and shareholder of the ResolveStroke startup and received speaker fees from Bracco. Other authors have no conflicts of interest to disclose.

Data availability statement

Data is available upon reasonable request.

Acknowledgments

The authors thank the Philippe Foundation, L'INSTITUT SERVIER, the French Society of Radiology for their support and J. Greig. The authors express their gratitude to the respective authors, publishers and journals for granting permission to use their images in this review.

Supplementary materials

Supplementary material associated with this article can be found in the online version at doi:10.1016/j.ultrasmedbio.2025.12.011.

References

[1] Guven G, Hilty MP, Ince C. Microcirculation: physiology, pathophysiology, and clinical application. Blood Purif 2020;49(1−2):143–50. doi: 10.1159/000503775.
[2] Cade WT. Diabetes-related microvascular and macrovascular diseases in the physical therapy setting. Phys Ther 2008;88(11):1322–35. doi: 10.2522/ptj.20080008.
[3] Goel S, Duda DG, Xu L, Munn LL, Boucher Y, Fukumura D, et al. Normalization of the vasculature for treatment of cancer and other diseases. Physiol Rev 2011;91 (3):1071–121. Erratum in: Physiol Rev. 2014 Apr;94(2):707. PMID: 21742796; PMCID: PMC3258432. doi: 10.1152/physrev.00038.2010.
[4] Greenberg SM. Small vessels, big problems. N Engl J Med 2006;354(14):1451–3. doi: 10.1056/NEJMp068043.
[5] Hanahan D, Weinberg RA. Hallmarks of cancer: the next generation. Cell 2011;144 (5):646–74. doi: 10.1016/j.cell.2011.02.013.
[6] Ooi QL, Tow FK, Deva R, Alias MA, Kawasaki R, Wong TY, et al. The microvasculature in chronic kidney disease. Clin J Am Soc Nephrol 2011;6(8):1872–8. Epub 2011 Jul 22. PMID: 21784828; PMCID: PMC3359539. doi: 10.2215/CJN.10291110.
[7] Gilson P, Merlin JL, Harlé A. Deciphering tumour heterogeneity: from tissue to liquid biopsy. Cancers 2022;14(6):1384. doi: 10.3390/cancers14061384.
[8] Wang HJ, Kjellstrand CM, Cockfield SM, Solez K. On the influence of sample size on the prognostic accuracy and reproducibility of renal transplant biopsy. Nephrol Dial Transplant 1998;13(1):165–72. doi: 10.1093/ndt/13.1.165.
[9] Lin E, Alessio A. What are the basic concepts of temporal, contrast, and spatial resolution in cardiac CT? J Cardiovasc Comput Tomogr 2009;3(6):403–8. doi: 10.1016/j.jcct.2009.07.003.
[10] Geethanath S, Vaughan JT. Accessible magnetic resonance imaging: a review. J Magn Reson Imaging JMRI 2019;49(7):e65–77. doi: 10.1002/jmri.26638.
[11] Diestro JDB, Omar 2nd AT, Zhang YQ, Kishibe T, Mastrolonardo A, Lannon MM, et al. Perfusion vs non-perfusion computed tomography imaging in the late window of emergent large vessel ischemic stroke: A systematic review and meta-analysis. PLoS One 2024;19(1):e0294127. PMID: 38166040; PMCID: PMC10760723. doi: 10.1371/journal.pone.0294127.
[12] Lamontagne-Caron R, Duchesne S. A scoping review of magnetic resonance angiography and perfusion image synthesis. Front Dement 2024;3:1408782. doi: 10.3389/frdem.2024.1408782.
[13] Christensen-Jeffries K, Couture O, Dayton PA, Eldar YC, Hynynen K, Kiessling F, et al. Super-resolution Ultrasound Imaging. Ultrasound Med Biol 2020;46(4):865–91. Epub 2020 Jan 21. PMID: 31973952; PMCID: PMC8388823. doi: 10.1016/j.ultrasmedbio.2019.11.013.
[14] Forsberg F, Kuruvilla B, Pascua MB, Chaudhari MH, Merton DA, Palazzo JP, et al. Comparing contrast-enhanced color flow imaging and pathological measures of breast lesion vascularity. Ultrasound Med Biol 2008;34(9):1365–72. Epub 2008 Apr 24. PMID: 18436369; PMCID: PMC2556965. doi: 10.1016/j.ultrasmedbio.2008.02.010.
[15] Lindner JR. Microbubbles in medical imaging: current applications and future directions. Nat Rev Drug Discov 2004;3(6):527–32. doi: 10.1038/nrd1417.
[16] Huang C, Zhang W, Gong P, Lok UW, Tang S, Yin T, et al. Super-resolution ultrasound localization microscopy based on a high frame-rate clinical ultrasound scanner: an in-human feasibility study. Phys Med Biol 2021;66(8). PMID: 33725687; PMCID: PMC8486312. doi: 10.1088/1361-6560/abef45.
[17] Desailly Y, Tissier AM, Correas JM, Wintzenrieth F, Tanter M, Couture O. Contrast enhanced ultrasound by real-time spatiotemporal filtering of ultrafast images. Phys Med Biol 2017;62(1):31–42. doi: 10.1088/1361-6560/62/1/31.
[18] Tinevez JY, Perry N, Schindelin J, Hoopes GM, Reynolds GD, Laplantine E, et al. TrackMate: An open and extensible platform for single-particle tracking. Methods 2017;115:80–90. Epub 2016 Oct 3. PMID: 27713081. doi: 10.1016/j.ymeth.2016.09.016.
[19] Andersen SB, Taghavi I, Søgaard SB, Hoyos CAV, Nielsen MB, Jensen JA, et al. Super-Resolution Ultrasound Imaging Can Quantify Alterations in Microbubble Velocities in the Renal Vasculature of Rats. Diagnostics (Basel) 2022;12(5):1111. PMID: 35626267; PMCID: PMC9140053. doi: 10.3390/diagnostics12051111.
[20] Errico C, Pierre J, Pezet S, Desailly Y, Lenkei Z, Couture O, et al. Ultrafast ultrasound localization microscopy for deep super-resolution vascular imaging. Nature 2015;527(7579):499–502. PMID: 26607546. doi: 10.1038/nature16066.
[21] Chabouh G, van Elburg B, Versluis M, Segers T, Quilliet C, Coupier G. Buckling of lipidic ultrasound contrast agents under quasi-static load. Philos Transact A Math Phys Eng Sci 2023;381(2244):20220025. doi: 10.1098/rsta.2022.0025.
[22] Dencks S, Schmitz G. Ultrasound localization microscopy. Z Med Phys 2023;33 (3):292–308. doi: 10.1016/j.zemedi.2023.02.004.
[23] Denis L, Bodard S, Hingot V, Chavignon A, Battaglia J, Renault G, et al. Sensing ultrasound localization microscopy for the visualization of glomeruli in living rats and humans. EBioMedicine 2023;91:104578. Epub 2023 Apr 20. PMID: 37086650; PMCID: PMC10149190. doi: 10.1016/j.ebiom.2023.104578.
[24] Chabouh G, Denis L, Abioui-Mourgues M, Deloges JB, Battaglia J, Chavignon A, et al. 3D transcranial ultrasound localization microscopy in awake mice: protocol and open-source pipeline. Commun Eng 2025;4(1):102. PMID: 40481246; PMCID: PMC12144258. doi: 10.1038/s44172-025-00415-4.
[25] Couture O, Hingot V, Heiles B, Muleki-Seya P, Tanter M. Ultrasound localization microscopy and super-resolution: a state of the art. IEEE Trans Ultrason Ferroelectr Freq Control 2018;65(8):1304–20. doi: 10.1109/TUFFC.2018.2850811.
[26] Song P, Rubin JM, Lowerison MR. Super-resolution ultrasound microvascular imaging: is it ready for clinical use? Z Med Phys 2023 S0939-3889(23)00043-0. doi: 10.1016/j.zemedi.2023.04.001.
[27] Xia S, Zheng Y, Hua Q, Wen J, Luo X, Yan J, et al. Chinese Artificial Intelligence Alliance for Thyroid and Breast Ultrasound. Super-resolution ultrasound and [microvasculomics] a consensus statement. Eur Radiol 2024 Nov;34 (11):7503–13. Epub 2024 May 29. PMID: 38811389. doi: 10.1007/s00330-024-10796-3.
[28] McInnes MDF, Moher D, Thombs BD, McGrath TA, Bossuyt PM, the PRISMA-DTA Group. et al. Preferred Reporting Items for a Systematic Review and Meta-analysis of Diagnostic Test Accuracy Studies: The PRISMA-DTA Statement. JAMA 2018 Jan 23;319(4):388–96. Erratum in: JAMA. 2019 Nov 26;322(20):2026. 10.1001/jama.2019.18307. PMID: 29362800. doi: 10.1001/jama.2017.19163.
[29] Yi HM, Lowerison MR, Song PF, Zhang W. A review of clinical applications for super-resolution ultrasound localization microscopy. Curr Med Sci 2022;42(1):1–16. doi: 10.1007/s11596-021-2459-2.
[30] Lo CKL, Mertz D, Loeb M. Newcastle-Ottawa scale: comparing reviewers' to authors' assessments. BMC Med Res Methodol 2014;14:45. doi: 10.1186/1471-2288-14-45.
[31] Sweeney MD, Kisler K, Montagne A, Toga AW, Zlokovic BV. The role of brain vasculature in neurodegenerative disorders. Nat Neurosci 2018;21(10):1318–31. doi: 10.1038/s41593-018-0234-x.
[32] Hoque MM, Abdelazim H, Jenkins-Houk C, Wright D, Patel BM, Chappell JC. The cerebral microvasculature: basic and clinical perspectives on stroke and glioma. Microcirc N Y N 1994 2021;28(3):e12671. doi: 10.1111/micc.12671.
[33] Ek Olofsson H, Englund E. A cortical microvascular structure in vascular dementia, Alzheimer's disease, frontotemporal lobar degeneration and nondemented controls: a sign of angiogenesis due to brain ischaemia? Neuropathol Appl Neurobiol 2019;45(6):557–69. doi: 10.1111/nan.12552.
[34] Brown WR, Thore CR. Review: cerebral microvascular pathology in ageing and neurodegeneration. Neuropathol Appl Neurobiol 2011;37(1):56–74. doi: 10.1111/j.1365-2990.2010.01139.x.
[35] Demené C, Robin J, Dizeux A, Heiles B, Pernot M, Tanter M, et al. Transcranial ultrafast ultrasound localization microscopy of brain vasculature in patients. Nat Biomed Eng 2021 Mar;5(3):219–28. Epub 2021 Mar 15. PMID: 33723412; PMCID: PMC7610356. doi: 10.1038/s41551-021-00697-x.
[36] Ultrasound super-resolution imaging of neonatal cerebral vascular reorganization during neurovascular interventions. 2023. Accessed February 1, 2025. https://society.org/articles/activity/10.21203/rs.3.rs-3660778/v1
[37] Regensburger AP, Wachter F, Denis L, Mandelbaum H, Schey F, Buehler A, et al. Ultrasound Localization Microscopy for the Assessment of Microvascular Circulation in Ischemic Perinatal Stroke. Stroke 2024 Dec;55(12):e323–5. Epub 2024 Oct 30. PMID: 39474686; PMCID: PMC11593985. doi: 10.1161/STROKEAHA.124.048390.
[38] Huang W, Hua C, Guo Y, Gao W, Li Y, Zheng Y. Super resolution imaging reconstruction reveals that gold standard methods may not correctly conclude neural/brain functional recovery. Comput Med Imaging Graph 2023;105:102198. doi: 10.1016/j.compmedimag.2023.102198.

[39] Denis L, Meseguer E, Gaudemer A, Jaklh G, Bodard S, Chabouh G, Hervé D, et al. Transcranial ultrasound localization microscopy in moyamoya patients using a clinical ultrasound system. Theranostics 2025;15(9):4074–83. PMID: 40213679; PMCID: PMC11980664. doi: 10.7150/thno.105427.
[40] Bourquin C, Poree J, Lesage F, Provost J. In vivo pulsatility measurement of cerebral microcirculation in rodents using dynamic ultrasound localization microscopy. IEEE Trans Med Imaging 2022;41(4):782–92. doi: 10.1109/TMI.2021.3123912.
[41] Hamaoka-Okamoto A, Suzuki C, Yahata T, Ikeda K, et al. The involvement of the vasa vasorum in the development of vasculitis in animal model of Kawasaki disease. Pediatr Rheumatol Online J 2014;12:12. PMID: 24678599; PMCID: PMC3986644. doi: 10.1186/1546-0096-12-12.
[42] Harky A, Fok M, Balmforth D, Bashir M. Pathogenesis of large vessel vasculitis: implications for disease classification and future therapies. Vasc Med Lond Engl 2019;24(1):79–88. doi: 10.1177/1358863×18802989.
[43] Goudot G, Jimenez A, Mohamedi N, Sitruk J, Khider L, Mortelette H, Papadacci C, et al. Assessment of Takayasu's arteritis activity by ultrasound localization microscopy. EBioMedicine 2023;90:104502. Epub 2023 Mar 7. PMID: 36893585; PMCID: PMC10017361. doi: 10.1016/j.ebiom.2023.104502.
[44] Goudot G, Jimenez A, Mohamedi N, Sitruk J, Wang LZ, Khider L, et al. Vasa vasorum interna in the carotid wall of active forms of Takayasu arteritis evidenced by ultrasound localization microscopy. Vasc Med 2024;29(3):296–301. Epub 2024 Mar 15. PMID: 38488572. doi: 10.1177/1358863X241228262.
[45] Leroy H, Wang LZ, Jimenez A, Mohamedi N, Papadacci C, Julia P, et al. Assessment of microvascular flow in human atherosclerotic carotid plaques using ultrasound localization microscopy. EBioMedicine 2025;111:105528. Epub 2024 Dec 26. PMID: 39729884; PMCID: PMC11733184. doi: 10.1016/j.ebiom.2024.105528.
[46] Skinner JS, Smeeth L, Kendall JM, Adams PC, Timmis A, Chest Pain Guideline Development Group. NICE Guidance. Chest pain of recent onset: assessment and diagnosis of recent onset chest pain or discomfort of suspected cardiac origin. Heart Br Card Soc 2010;96(12):974–8. doi: 10.1136/hrt.2009.190066.
[47] Yan J, Huang B, Tonko J, Toulemonde M, Hansen-Shearer J, Tan Q, et al. Transthoracic ultrasound localization microscopy of myocardial vasculature in patients. Nat Biomed Eng 2024;8(6):689–700. Epub 2024 May 6. PMID: 38710839; PMCID: PMC11250254. doi: 10.1038/s41551-024-01206-6.
[48] Demené C, Deffieux T, Pernot M, Osmanski BF, Biran V, Gennisson JL, et al. Spatiotemporal Clutter Filtering of Ultrafast Ultrasound Data Highly Increases Doppler and fUltrasound Sensitivity. IEEE Trans Med Imaging 2015;34(11):2271–85. Epub 2015 Apr 30. PMID: 25955583. doi: 10.1109/TMI.2015.2428634.
[49] Basile DP, Yoder MC. Renal endothelial dysfunction in acute kidney ischemia reperfusion injury. Cardiovasc Hematol Disord Drug Targets 2014;14(1):3–14. doi: 10.2174/1871529×1401140724093505.
[50] Kwiatkowska E, Kwiatkowski S, Dziedziejko V, Tomasiewicz I, Domański L. Renal microcirculation injury as the main cause of ischemic acute kidney injury development. Biology 2023;12(2):327. doi: 10.3390/biology12020327.
[51] Pollak MR, Quaggin SE, Hoenig MP, Dworkin LD. The glomerulus: the sphere of influence. Clin J Am Soc Nephrol CJASN 2014;9(8):1461–9. doi: 10.2215/CJN.09400913.
[52] Kanzaki G, Tsuboi N, Shimizu A, Yokoo T. Human nephron number, hypertension, and renal pathology. Anat Rec Hoboken NJ 2007 2020;303(10):2537–43. doi: 10.1002/ar.24302.
[53] Tonneijck L, Muskiet MH, Smits MM, van Bommel EJ, Heerspink HJ, van Raalte DH, et al. Glomerular Hyperfiltration in Diabetes: Mechanisms, Clinical Significance, and Treatment. J Am Soc Nephrol 2017;28(4):1023–39. Epub 2017 Jan 31. PMID: 28143897; PMCID: PMC5373460. doi: 10.1681/ASN.2016060666.
[54] Segelmark M, Hellmark T. Autoimmune kidney diseases. Autoimmun Rev 2010;9(5):A366–71. doi: 10.1016/j.autrev.2009.11.007.
[55] Denic A, Elsherbiny H, Rule AD. In-vivo techniques for determining nephron number. Curr Opin Nephrol Hypertens 2019;28(6):545–51. doi: 10.1097/MNH.0000000000000540.
[56] Bennett KM, Baldelomar EJ, Morozov D, Chevalier RL, Charlton JR. New imaging tools to measure nephron number in vivo: opportunities for developmental nephrology. J Dev Orig Health Dis 2021;12(2):179–83. doi: 10.1017/S204017442000001X.
[57] Bodard S, Denis L, Chabouh G, Battaglia J, Anglicheau D, Hélénon O, et al. Visualization of Renal Glomeruli in Human Native Kidneys With Sensing Ultrasound Localization Microscopy. Invest Radiol 2024;59(8):561–8. Epub 2024 Jan 12. PMID: 38214557. doi: 10.1097/RLI.0000000000001061.
[58] Barinotti A, Radin M, Cecchi I, Foddai SG, Rubini E, Roccatello D, et al. Serum Biomarkers of Renal Fibrosis: A Systematic Review. Int J Mol Sci 2022;23(22):14139. PMID: 36430625; PMCID: PMC9697720. doi: 10.3390/ijms232214139.
[59] Najafian B, Lusco MA, Alpers CE, Fogo AB. Approach to kidney biopsy: core curriculum 2022. Am J Kidney Dis 2022;80(1):119–31. doi: 10.1053/j.ajkd.2021.08.024.
[60] Chen Q, George MW, McMahon B, Rosenthal JA, Kim K, Tan RJ. Super-resolution ultrasound to assess kidney vascular changes in humans with kidney disease. Am J Kidney Dis 2024 S0272-6386(24)00923-5. doi: 10.1053/j.ajkd.2024.06.021.
[61] Bodard S, Denis L, Hingot V, Chavignon A, Hélénon O, Anglicheau D, et al. Ultrasound localization microscopy of the human kidney allograft on a clinical ultrasound scanner. Kidney Int 2023;103(5):930–5. Epub 2023 Feb 24. PMID: 36841476. doi: 10.1016/j.kint.2023.01.027.
[62] Grieshaber-Bouyer Mandelbaum H, Wachter F, Denis L, Reisinger C, Buehler A, Yan J, et al. Sensing ultrasound localization microscopy for ultrastructural and functional imaging of neonatal kidneys. Ultraschall Med 2025 English. Epub ahead of print. PMID: 41130267. doi: 10.1055/a-2700-9184.
[63] Huang X, Zhang Y, Zhou Q, Deng Q. Value of ultrasound super-resolution imaging for the assessment of renal microcirculation in patients with acute kidney injury: a preliminary study. Diagn Basel Switz 2024;14(11):1192. doi: 10.3390/diagnostics14111192.
[64] Yoon SY, Kim JS, Jeong KH, Kim SK. Acute kidney injury: biomarker-guided diagnosis and management. Med Kaunas Lith 2022;58(3):340. doi: 10.3390/medicina58030340.
[65] Huang C, Wai Lok U, Zhang J, Zhu XY, Krier JD, Stern A, et al. Optimizingin vivo-data acquisition for robust clinical microvascular imaging using ultrasound localization microscopy. Phys Med Biol 2025;70(7). PMID: 40086078; PMCID: PMC12010384. doi: 10.1088/1361-6560/adc0de.
[66] Tharakan T, Luo R, Jayasena CN, Minhas S. Non-obstructive azoospermia: current and future perspectives. Fac Rev 2021;10:7. doi: 10.12703/r/10-7.
[67] Takeshima T, Karibe J, Saito T, Kuroda S, Komeya M, Uemura H, et al. Clinical management of nonobstructive azoospermia: An update. Int J Urol 2024;31(1):17–24. Epub 2023 Sep 22. PMID: 37737473. doi: 10.1111/iju.15301.
[68] Minhas S, Bettocchi C, Boeri L, Capogrosso P, Carvalho J, Cilesiz NC, et al. EAU Working Group on Male Sexual and Reproductive Health. European Association of Urology Guidelines on Male Sexual and Reproductive Health: 2021 Update on Male Infertility. Eur Urol 2021;80(5):603–20. Epub 2021 Sep 10. PMID: 34511305. doi: 10.1016/j.eururo.2021.08.014.
[69] Practice Committee of American Society for Reproductive Medicine. Multiple gestation associated with infertility therapy: an American Society for Reproductive Medicine Practice Committee opinion. Fertil Steril 2012;97(4):825–34. doi: 10.1016/j.fertnstert.2011.11.048.
[70] Moon MH, Kim SH, Cho JY, Seo JT, Chun YK. Scrotal US for evaluation of infertile men with azoospermia. Radiology 2006;239(1):168–73. doi: 10.1148/radiol.2391050272.
[71] Andrade DL, Viana MC, Esteves SC. Differential diagnosis of azoospermia in men with infertility. J Clin Med 2021;10(14):3144. doi: 10.3390/jcm10143144.
[72] Li M, Chen L, Yan J, Jayasena CN, Liu Z, Li J, et al. Super-resolution ultrasound localization microscopy for the non-invasive imaging of human testicular microcirculation and its differential diagnosis role in male infertility. VIEW 2024;5(2):20230093. doi: 10.1002/VIW.20230093.
[73] Li M, Zhang X, Yan J, Shu H, Li Z, Ye C, et al. Non-invasive ultrasound localization microscopy (ULM) in azoospermia: connecting testicular microcirculation to spermatogenic functions. Theranostics 2024;14(13):4967–82. PMID: 39267788; PMCID: PMC11388075. doi: 10.7150/thno.99668.
[74] Solomon O, van Sloun RJG, Wijkstra H, Mischi M, Eldar YC. Exploiting flow dynamics for superresolution in contrast-enhanced ultrasound. IEEE Trans Ultrason Ferroelectr Freq Control 2019;66(10):1573–86. doi: 10.1109/TUFFC.2019.2926062.
[75] Kanoulas E, Butler M, Rowley C, Voulgaridou V, Diamantis K, Duncan WC, et al. Super-Resolution Contrast-Enhanced Ultrasound Methodology for the Identification of In Vivo Vascular Dynamics in 2D. Invest Radiol 2019;54(8):500–16. PMID: 31058661; PMCID: PMC6661242. doi: 10.1097/RLI.0000000000000565.
[76] Morris M, Durie E, Sinnett V, Toulemonde M, Roxanis I, Allen S, et al. In-Patient repeatability and sensitivity study of multi-plane super-resolution ultrasound in breast cancer. medRxiv 2024. doi: 10.1101/2024.10.15.24315514.
[77] Gerwing M, Herrmann K, Helfen A, Schliemann C, Berdel WE, Eisenblätter M, et al. The beginning of the end for conventional RECIST - novel therapies require novel imaging approaches. Nat Rev Clin Oncol 2019;16(7):442–58 PMID: 30718844. doi: 10.1038/s41571-019-0169-5.
[78] Ko CC, Yeh LR, Kuo YT, Chen JH. Imaging biomarkers for evaluating tumor response: RECIST and beyond. Biomark Res 2021;9(1):52. doi: 10.1186/s40364-021-00306-8.
[79] Carmeliet P, Jain RK. Angiogenesis in cancer and other diseases. Nature 2000;407(6801):249–57. doi: 10.1038/35025220.
[80] Farnsworth RH, Lackmann M, Achen MG, Stacker SA. Vascular remodeling in cancer. Oncogene 2014;33(27):3496–505. doi: 10.1038/onc.2013.304.
[81] Ehling J, Theek B, Gremse F, Baetke S, Möckel D, Maynard J, et al. Micro-CT imaging of tumor angiogenesis: quantitative measures describing micromorphology and vascularization. Am J Pathol 2014;184(2):431–41. Epub 2013 Nov 18. PMID: 24262753; PMCID: PMC3920056. doi: 10.1016/j.ajpath.2013.10.014.
[82] Walsh JC, Lebedev A, Aten E, Madsen K, Marciano L, Kolb HC. The clinical importance of assessing tumor hypoxia: relationship of tumor hypoxia to prognosis and therapeutic opportunities. Antioxid Redox Signal 2014;21(10):1516–54. doi: 10.1089/ars.2013.5378.
[83] Tolaney SM, Boucher Y, Duda DG, Martin JD, Seano G, Ancukiewicz M, et al. Role of vascular density and normalization in response to neoadjuvant bevacizumab and chemotherapy in breast cancer patients. Proc Natl Acad Sci U S A 2015;112(46):14325–30. Epub 2015 Nov 2. PMID: 26578779; PMCID: PMC4655544. doi: 10.1073/pnas.1518808112.
[84] Bullitt E, Lin NU, Ewend MG, Zeng D, Winer EP, Carey LA, et al. Tumor therapeutic response and vessel tortuosity: preliminary report in metastatic breast cancer. Med Image Comput Comput Assist Interv 2006;9(Pt 2):561–8. PMID: 17354817; PMCID: PMC2504703. doi: 10.1007/11866763_69.
[85] Deering RE, Bigler SA, Brown M, Brawer MK. Microvascularity in benign prostatic hyperplasia. The Prostate 1995;26(3):111–5. doi: 10.1002/pros.2990260302.
[86] Salomao DR, Graham SD, Bostwick DG. Microvascular invasion in prostate cancer correlates with pathologic stage. Arch Pathol Lab Med 1995;119(11):1050–4.
[87] Dencks S, Piepenbrock M, Opacic T, Krauspe B, Stickeler E, Kiessling F, et al. Clinical Pilot Application of Super-Resolution US Imaging in Breast Cancer. IEEE Trans Ultrason Ferroelectr Freq Control 2019;66(3):517–26. Epub 2018 Sep 24. PMID: 30273150. doi: 10.1109/TUFFC.2018.2872067.
[88] Opacic T, Dencks S, Theek B, Piepenbrock M, Ackermann D, Rix A, et al. Motion model ultrasound localization microscopy for preclinical and clinical multiparametric tumor characterization. Nat Commun 2018;9(1):1527. PMID: 29670096; PMCID: PMC5906644. doi: 10.1038/s41467-018-03973-8.
[89] Lei YM, Liu C, Hu HM, Li N, Zhang N, Wang Q, et al. Combined use of super-resolution ultrasound imaging and shear-wave elastography for differential diagnosis of

breast masses. Front Oncol 2024;14:1497140. PMID: 39759128; PMCID: PMC11695221. doi: 10.3389/fonc.2024.1497140.
[90] Li J, Chen L, Wang R, Zhu J, Li A, Li J, et al. Ultrasound localization microscopy in the diagnosis of breast tumors and prediction of relevant histologic biomarkers associated with prognosis in humans: the protocol for a prospective, multicenter study. BMC Med Imaging 2025;25(1):13. PMID: 39780089; PMCID: PMC11715691. doi: 10.1186/s12880-024-01535-7.
[91] Zeng QQ, An SZ, Chen CN, Wang Z, Liu JC, Wan MX, et al. Focal liver lesions: multiparametric microvasculature characterization via super-resolution ultrasound imaging. Eur Radiol Exp 2024 Dec 5;8(1):138. PMID: 39636384; PMCID: PMC11621259. doi: 10.1186/s41747-024-00540-3.
[92] Bodard S, Denis L, Chabouh G, Anglicheau D, Hélénon O, Correas JM, et al. First clinical utility of sensing Ultrasound Localization Microscopy (sULM): identifying renal pseudotumors. Theranostics 2025;15(1):233–44. PMID: 39744234; PMCID: PMC11667240. doi: 10.7150/thno.100897.
[93] Hansen-Shearer J, Yan J, Lerendegui M, Huang B, Toulemonde M, Riemer K, et al. Ultrafast 3-D Transcutaneous Super Resolution Ultrasound Using Row-Column Array Specific Coherence-Based Beamforming and Rolling Acoustic Sub-aperture Processing: In Vitro, in Rabbit and in Human Study. Ultrasound Med Biol 2024;50(7):1045–57. Epub 2024 May 3. PMID: 38702285. doi: 10.1016/j.ultrasmedbio.2024.03.020.
[94] Zhu J, Zhang C, Christensen-Jeffries K, Zhang G, Harput S, Dunsby C, et al. Super-Resolution Ultrasound Localization Microscopy of Microvascular Structure and Flow for Distinguishing Metastatic Lymph Nodes - An Initial Human Study. Ultraschall Med 2022;43(6):592–8. English. Epub 2022 Oct 7. PMID: 36206774. doi: 10.1055/a-1917-0016.
[95] Beliard B, Ahmanna C, Tiran E, Kanté K, Deffieux T, Tanter M, et al. Ultrafast Doppler imaging and ultrasound localization microscopy reveal the complexity of vascular rearrangement in chronic spinal lesion. Sci Rep 2022;12(1):6574. PMID: 35449222; PMCID: PMC9023600. doi: 10.1038/s41598-022-10250-8.
[96] Huang C, Lowerison MR, Trzasko JD, Manduca A, Bresler Y, Tang S, et al. Short Acquisition Time Super-Resolution Ultrasound Microvessel Imaging via Microbubble Separation. Sci Rep 2020;10(1):6007. PMID: 32265457; PMCID: PMC7138805. doi: 10.1038/s41598-020-62898-9.
[97] Heiles B, Correia M, Hingot V, Pernot M, Provost J, Tanter M, et al. Ultrafast 3D Ultrasound Localization Microscopy Using a 32 × 32 Matrix Array. IEEE Trans Med Imaging 2019;38(9):2005–15. Epub 2019 Apr 1. PMID: 30946662. doi: 10.1109/TMI.2018.2890358.
[98] Porte C, Lisson T, Kohlen M, von Maltzahn F, Dencks S, von Stillfried S, et al. Ultrasound Localization Microscopy for Breast Cancer Imaging in Patients: Protocol Optimization and Comparison with Shear Wave Elastography. Ultrasound Med Biol 2024;50(1):57–66. Epub 2023 Oct 6. PMID: 37805359. doi: 10.1016/j.ultrasmedbio.2023.09.001.
[99] Hingot V, Errico C, Heiles B, Rahal L, Tanter M, Couture O. Microvascular flow dictates the compromise between spatial resolution and acquisition time in ultrasound localization microscopy. Sci Rep 2019;9(1):2456. doi: 10.1038/s41598-018-38349-x.
[100] Harput S, Christensen-Jeffries K, Brown J, Li Y, Williams KJ, Davies AH, et al. Two-Stage Motion Correction for Super-Resolution Ultrasound Imaging in Human Lower Limb. IEEE Trans Ultrason Ferroelectr Freq Control 2018;65(5):803–14. PMID: 29733283. doi: 10.1109/TUFFC.2018.2824846.
[101] Denis L, Chabouh G, Heiles B, Couture O. Volumetric ultrasound localization microscopy. IEEE Trans Ultrason Ferroelectr Freq Control 2024. doi: 10.1109/TUFFC.2024.3485556.
[102] Bazan R, Braga GP, Luvizutto GJ, Hueb JC, Hokama NK, Zanati Bazan SG, et al. Evaluation of the Temporal Acoustic Window for Transcranial Doppler in a Multi-Ethnic Population in Brazil. Ultrasound Med Biol 2015;41(8):2131–4. Epub 2015 May 9. PMID: 25964064. doi: 10.1016/j.ultrasmedbio.2015.04.008.
[103] Lambert W, Cobus LA, Robin J, Fink M, Aubry A. Ultrasound matrix imaging-part II: the distortion matrix for aberration correction over multiple isoplanatic patches. IEEE Trans Med Imaging 2022;41(12):3921–38. doi: 10.1109/TMI.2022.3199483.
[104] Xing P, Poree J, Rauby B, Malescot A, Martineau E, Perrot V, et al. Phase aberration correction for in vivo ultrasound localization microscopy using a spatio-temporal complex-valued neural network. IEEE Trans Med Imaging 2024;43(2):662–73. doi: 10.1109/TMI.2023.3316995.
[105] Chavignon A, Hingot V, Orset C, Vivien D, Couture O. 3D transcranial ultrasound localization microscopy for discrimination between ischemic and hemorrhagic stroke in early phase. Sci Rep 2022;12(1):14607. doi: 10.1038/s41598-022-18025-x.
[106] Chabouh G, Denis L, Bodard S, Lager F, Renault G, Chavignon A, et al. Whole Organ Volumetric Sensing Ultrasound Localization Microscopy for Characterization of Kidney Structure. IEEE Trans Med Imaging 2024;43(11):4055–63. Epub 2024 Nov 4. PMID: 38857150. doi: 10.1109/TMI.2024.3411669.
[107] Dencks S, Lisson T, Oblisz N, Kiessling F, Schmitz G. Ultrasound localization microscopy precision of clinical 3-D ultrasound systems. IEEE Trans Ultrason Ferroelectr Freq Control 2024;71:1677–89. doi: 10.1109/TUFFC.2024.3467391.
[108] Jia WR, Tang L, Wang DB, Chai WM, Fei XC, He JR, et al. Three-dimensional Contrast-enhanced Ultrasound in Response Assessment for Breast Cancer: A Comparison with Dynamic Contrast-enhanced Magnetic Resonance Imaging and Pathology. Sci Rep. 2016;6:33832 PMID: 27652518; PMCID: PMC5031978. doi: 10.1038/srep33832.
[109] Favre H, Pernot M, Tanter M, Papadacci C. Boosting transducer matrix sensitivity for 3D large field ultrasound localization microscopy using a multi-lens diffracting layer: a simulation study. Phys Med Biol 2022;67(8). doi: 10.1088/1361-6560/ac5f72.